

Study of Forces and Dynamic Coefficients in Whirling and Eccentric Labyrinth Seals Using ANSYS-CFX

Elizabeth D. Thompson

Thesis submitted to the faculty of the Virginia Polytechnic Institute and State University in
partial fulfillment of the requirements for the degree of

Master of Science
in
Mechanical Engineering

R. Gordon Kirk, Chair

Mary Kasarda

Bob West

April 28, 2009
Blacksburg, Virginia

Keywords: Labyrinth Seal, ANSYS-CFX, Whirl Speed Study, Eccentricity Study

Study of Forces and Dynamic Coefficients in Whirling and Eccentric Labyrinth Seals Using ANSYS-CFX

Elizabeth D. Thompson

Abstract

Labyrinth seal force estimates are important to the prediction of the stability of turbomachinery. The force prediction methods fall into several categories: experiments, bulk flow analysis, and finite volume analysis. Finite volume analysis can be split into two subcategories: self-developed and commercial.

In this research, a commercial computational fluid dynamics (CFD) program called ANSYS-CFX was used to predict the forces generated in a labyrinth seal whirling at specified speeds. The results were compared to data from VT-FAST, a bulk flow code, and TASCflow, another commercial CFD program. It was shown that there were discrepancies among the results, and several hypotheses were made as to the reason for these discrepancies.

Additionally, ANSYS-CFX was used to study the effect of labyrinth seal eccentricity ratio on the resultant force generated. It was shown that the radial force component within the seal behaved linearly with respect to eccentricity ratio. However, the tangential force component had no distinguishable relationship with the eccentricity ratio. It was hypothesized that the lack of a relationship was caused by the small fluctuations in the inlet swirl. Although the inlet swirl varied very little at each eccentricity ratio, it was shown there was a relationship between the tangential force and inlet swirl.

Acknowledgements

I would first like to thank my advisor Dr. R. Gordon Kirk for imparting a portion of his vast rotordynamic knowledge on me, and for supporting me throughout the research and thesis writing processes. I would also like to thank Dr. Mary Kasarda and Dr. Bob West for serving on my advisory committee and gracefully handling the scheduling and thesis curveballs during the past semester.

Additionally, I'd like to express my gratitude to the other members of the Virginia Tech Rotordynamics Laboratory, especially Dr. Zenglin Guo, for their help over the last two years. I'd like to acknowledge the Rotordynamics Laboratory Affiliates Group for the sponsorship of this research.

I would like to say a huge thank you to my parents for all their love and support throughout my education, and for nodding along and pretending to understand the long winded explanations of my research. Also: Mom – thanks for answering my grammar questions (I is an engineer), and Dad – thanks for giving me a fresh perspective on my thesis. Last, but most certainly not least, I'd like thank Pierce for all his love, support, revision help, thesis text recovery, and for providing copious amounts of ice cream.

Table of Contents

List of Figures	vi
List of Tables	viii
Nomenclature	ix
Section 1: Introduction and Literature Review	1
1.1 Labyrinth Seal Background	1
1.2 Past Work	2
Section 2: API Seal Introduction	6
2.1 Purpose of API Study	6
2.2 Results of Study	6
2.3 Labyrinth Seal Characteristics	6
2.4 API Seal Modifications	7
Section 3: Tooth-on-Stator Seal Characteristics	9
3.1 Model	9
3.2 Mesh	10
3.2.1 CFX-Mesh Procedure	10
3.2.2 CFX-Mesh Advantages and Drawbacks	11
3.3 Pre-Processing	11
3.4 Solution Procedure	12
3.4.1 Node Increase Method	12
3.4.2 Laminar/Turbulent Method	13
3.4.3 Discussion	13
3.5 Solution Times	13
3.5.1 Whirl Speed Study	14
3.5.2 Eccentric Study	15
3.6 Post Processing	15
Section 4: Whirl Speed Variation Within ANSYS-CFX	17
4.1 Purpose	17
4.2 Results	17
4.3 Comparison of CFX Results to Bulk Flow and TASCflow Results	23

4.4	Comparison of CFX Results to LabyXL Results.....	25
Section 5:	Eccentricity Variation Within ANSYS-CFX.....	26
5.1	Purpose.....	26
5.2	Results.....	26
5.3	Comparison to Published Data.....	35
Section 6:	Summary and Conclusion.....	38
6.1	Whirl Speed Study	38
6.2	Eccentric Study	39
6.3	Future Work and Recommendations	40
References.....		41
Appendix A:	Solution Run Times.....	43
Appendix B:	Whirl Speed Variation Study Flow Characteristics	46
Appendix C:	Eccentricity Variation Study Flow Characteristics	51

List of Figures

Figure	Caption	Page
1-1	Labyrinth Types: (a) Tooth-on-Stator Straight Labyrinth; (b) Staggered Labyrinth; (c) Full Labyrinth.	1
2-1	API Seal Geometry	7
2-2	Modified API Seal with Added Pre-Seal Flow Path	8
3-1	Pictorial Representation of Angular Resolution	11
3-2	Rotating Reference Frame	12
3-3	Whirl Speed Versus Time to Solution for the Whirl Speed Study	14
3-4	Eccentricity Ratio Versus Time to Solution for the Eccentric Study	15
4-1	Full Whirl Speed Study Flow Path	18
4-2	Whirl Speed Study Flow Path Cutaway	18
4-3	Inlet Pressure Versus Whirl Speed	19
4-4	Percent Difference from Inlet Pressure Target Value Versus Whirl Speed	19
4-5	Rotor Force Representation	21
4-6	Radial Force on the Rotor Versus Whirl Speed	22
4-7	Tangential Force on the Rotor Versus Whirl Speed	22
4-8	Radial Force/ δ Versus Whirl Speed	24
4-9	Tangential Force/ δ Versus Whirl Speed	24
5-1	Full Eccentric Study Flow Path	27
5-2	Eccentric Study Flow Path Cutaway	27
5-3	Actual Inlet Pressure Versus Eccentricity Ratio	28
5-4	Inlet Pressure Percent Difference from Target Versus Eccentricity Ratio	28
5-5	Percent Inlet Swirl Versus Eccentricity Ratio	29
5-6	Circumferential Pressure Versus Theta	30
5-7	Circumferential Velocity Versus Theta	30
5-8	Radial Force Versus Eccentricity Ratio	31
5-9	Tangential Force Versus Eccentricity Ratio	32
5-10	Direct Stiffness Versus Eccentricity Ratio	33
5-11	Cross-coupled Stiffness Versus Eccentricity Ratio	33

5-12	Direct Damping Versus Eccentricity Ratio	34
5-13	Cross-coupled Damping Versus Eccentricity Ratio	34
5-14	Variation of Normalized Tangential Force and the Inverse Normalized Inlet Swirl With Respect to Eccentricity Ratio	36
B-1	Pressure Contour of the Entire Seal	46
B-2	Pressure Contour of API Seal	47
B-3	Stationary Frame Velocity Contours	48
B-4	Stationary Frame Velocity Vectors	49
B-5	Stationary Frame Velocity Streamlines Between Second and Third Teeth	50
C-1	Full Seal Pressure Distribution	51
C-2	API Seal Pressure Distribution	52
C-3	Stationary Frame Velocity Contours	53
C-4	Stationary Frame Velocity Vectors	54
C-5	Stationary Frame Velocity Streamlines Between Third and Fourth Teeth	55

List of Tables

Table	Caption	Page
2-1	API Seal Geometric Dimensions	7
2-2	API Seal Operating Conditions	7
3-1	Pre-Seal Geometric Characteristics	9
3-2	Pre-Seal Inlet Conditions	10
4-1	Dynamic Coefficients	23
5-1	Dynamic Coefficients for Varying Eccentricity Ratios	35
6-1	CFX Dynamic Coefficients	38
6-2	CFX Dynamic Coefficients for Varying Eccentricity Ratios	39
A-1	Run Data for the Whirl Speed Study	43
A-2	Run Data for the Eccentricity Study	44

Nomenclature

		Subscripts
A	Area, m ²	
C	Direct Damping, N-s/m	r Radial Direction
c	Cross-Coupled Damping, N-s/m	t Tangential Direction
D _s	Seal Diameter, mm	x x-direction
D _{ps}	Pre-seal Diameter, mm	y y-direction
δ	Eccentricity, mm	z z-direction
ε	Eccentricity Ratio	
F	Force, N	
h	Radial Clearance, mm	
K	Direct Stiffness, N/m	
k	Cross-Coupled Stiffness, N/m	
L	Horizontal Spacing, mm	
L _{ent}	Entry Length, mm	
n	Normal	
Ω	Rotational Speed, rad/s	
ω	Whirl Speed, rad/s	
ω _{Ncr}	Critical Speed, rad/s	
P	Pressure, Pa	
Q _e	Effective Stiffness, N/m	
T _e	Tooth Exit/Entry Spacing, mm	
T _h	Tooth Height, mm	
T _s	Tooth Pitch, mm	
T _w	Tooth Tip Width, mm	

Section 1: Introduction and Literature Review

1.1 Labyrinth Seal Background

Labyrinth seals are non-contacting annular gas seals and are typically found in gas compressors and turbines. They are used to reduce leakage and facilitate a pressure drop from a region of high pressure into a region of lower pressure. This is accomplished by creating a flow path for the working fluid that converts the pressure head into kinetic energy. The kinetic energy is then dissipated. There are several basic geometries: straight, staggered, and full. Representations of these geometries are in Figure 1-1. The straight labyrinth can be split into several categories: tooth-on-stator and tooth-on-rotor.

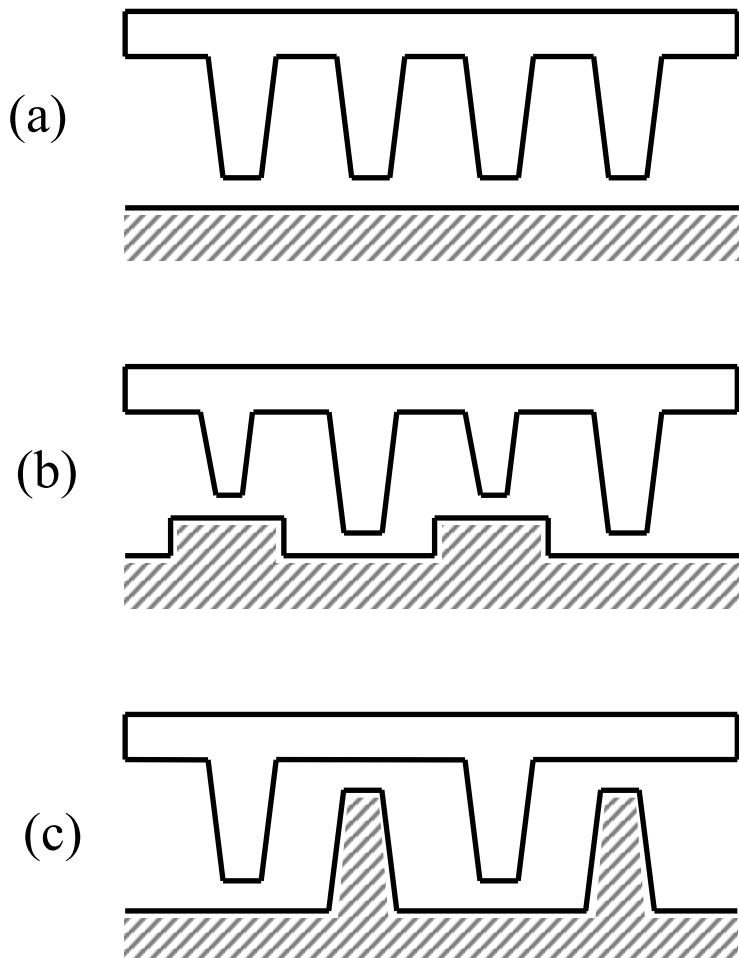


Figure 1-1. Labyrinth Types: (a) Tooth-on-Stator Straight Labyrinth; (b) Staggered Labyrinth; (c) Full Labyrinth.

1.2 Past Work

The study of labyrinth seals has progressed over the years. There were several major stages in the development of methods to study the forces and dynamic characteristics of the seals: experiments, bulk flow, and finite volume methods. Each stage led to new understanding about the behavior of labyrinth seals.

Originally, most of the work focused upon experimental data and simplified rotordynamic systems. Alford [1] studied a labyrinth seal with varying inlet and outlet areas. He concluded that when the inlet area exceeds the outlet area, an excitation force is produced that causes whirl in the direction of the rotation. Conversely, Alford concluded that no excitation force will be produced when the outlet area exceeds the inlet area.

More experimental work was carried out by Bencker and Wachter [2]. They calculated spring coefficients for the seals, but in later years, these results have been called into question [3]. Although the spring coefficients were called into question, Bencker and Wachter's overall theory of labyrinth seals is still considered valid. It was concluded that the tangential forces in eccentric labyrinth seals result from an uneven circumferential pressure distribution in the seal, which was found to be induced by circumferential flow within the seal. The circumferential flow comes from two sources: shaft rotation and swirling flows at the entrance to the seal. It was shown with a variety of seals that the tangential forces are linear with respect to the eccentricity ratio of the seal.

Rajakumar and Sisto [4] more recently performed experiments to determine the circumferential pressure distributions and forces within a labyrinth seal. They studied the variation of the radial and tangential forces with respect to eccentricity ratio and rotor speed, both with and without inlet swirl. It was shown that the dominant influence on forward whirl in short labyrinth seals is inlet swirl. Additionally, it was shown that the magnitude of the radial force increases when there is inlet swirl in an eccentric seal.

Starting in the 1980s, more robust methods were brought into use to study the dynamic characteristics of labyrinth seals. There were two main methods used: bulk flow and finite

volume. Wyssmann et al. [5] used a two control volume approach to model the flow through a labyrinth seal. The two control volume approach is a simplified approach to a finite volume method. For that reason, the modeled flow through the seal was oversimplified and can only be used for general comparisons and trends.

Rhode and Sobolik [6] used a finite difference approximation to predict the leakage flow through a labyrinth seal. Their model contained one cavity that was used iteratively to model the flow though labyrinth seals with five, ten, and fifteen cavities. Their computer code was validated with other types of flows, including subsonic flow through a pipe expansion and incompressible flow though a large scale model of a generic labyrinth seal. It was shown that relatively close agreement with experimental labyrinth seal data was achieved with the fifteen cavity seal. Flow characteristics within a single labyrinth cavity were also shown.

With the improvement of personal computers, more advanced finite volume codes were developed and used by Rhode et al. [7], Ishii et al. [8], and Moore [9]. Rhode et al. [7] again developed and used their own finite volume code to study the flow through labyrinth seals. Rhode et al. [7] studied the influence of inlet swirl on the flow though a labyrinth seal. They showed that the inlet swirl has a significant influence on the forces produced. Larger inlet swirls increased the forces produced, and led to more unstable operating conditions.

Ishii et al. [8] developed and used a finite volume solver to find the flow and rotordynamic forces in a labyrinth seal. They demonstrated that the produced circumferential pressure distribution had good agreement with experimental data. Additionally, it was shown the inlet swirl caused less desirable radial and tangential forces in the labyrinth seal. It was determined that the finite volume code calculated forces that had good agreement with experimental data for the interior labyrinth seal cavities, but did not agree well with the experimental results for the cavities towards the inlet and outlet of the labyrinth seal.

Moore [9] developed a computational fluid dynamics (CFD) code to analyze the flow and forces in a labyrinth seal. The CFD results were compared to bulk flow codes and it was shown that the bulk flow codes under-predicted direct stiffness values and reasonably predicted damping values.

It was noted that the CFD results correlate well with experimental results for forces and leakage. Additionally, it was observed that compared to the bulk flow codes, a drawback to the CFD software is the greater computational time involved in obtaining CFD solutions.

Kirk [3] developed a bulk flow code to determine the dynamic characteristics of a labyrinth seal. The code was originally called DYNLAB, but has since been renamed VT-FAST [10], and most recently has been integrated with Microsoft Excel and renamed LabyXL [11]. LabyXL was created to streamline the usage of VT-FAST for gas labyrinth seals. Both a pre-processor and a post-processor were created using Visual Basic for Applications to integrate LabyXL with Microsoft Excel [11].

Kocur et al. [12] analyzed the results of an American Petroleum Institute (API) survey of gas labyrinth seal and tilting pad journal bearing dynamic coefficient predictions from various analysis codes. The intent was to assess the variation in dynamic coefficients predicted by different analysis codes. It was noted in this study that an incorrect value of the first critical speed was given in the API survey. It was shown there was a large amount of variability in the provided dynamic coefficients. This variability led the authors to state that a new standard for experimental data is needed, so the data could be used to verify the analytical results. The authors noted that the labyrinth seal radial force coefficients were ignored in the study because there were large variations in the coefficients.

Commercial CFD programs have also been used to study the flow and resulting forces within labyrinth seals. Kirk and Guo [13] used ANSYS-TASCflow to produce labyrinth seal forces and flow properties. These results were compared to bulk flow results from DYNLAB. For an isolated labyrinth seal with no inlet swirl, it was demonstrated that the bulk flow code produced larger seal forces than the CFD code. A leak path was added to the labyrinth geometry in an attempt to fully model the labyrinth seal flow path. It was shown that it was possible to come close to the CFD results by varying the friction factors of the bulk flow code. Kirk and Guo [13] also evaluated the labyrinth seal flow in a high speed compressor. It was shown that for the high speed compressor, there was good agreement between the TASCflow and bulk flow leakage results. As was shown in the previous case, the bulk flow cavity swirl results can be matched to

the TASCflow swirl results by varying the bulk flow code friction factors. Overall, it was shown that the bulk flow code produced more destabilizing forces when compared to the TASCflow force results.

Hirano et al. [14] again used TASCflow to model the flow though a labyrinth seal, and compared the results to DYNLAB results. In this paper, a mesh density study was performed to look at the effect of mesh density on the solution. Ideally, CFD results should be independent of the mesh used. The flow between teeth was split into 4 regions. There were three regions in each chamber and one region between the rotor and the tip of the tooth. Each region was analyzed until a result independent mesh was found for each region. Most notably, the mesh density study was performed at zero inlet swirl. The result independent mesh was used to obtain results that could be compared to the DYNLAB bulk flow results. It was shown that TASCflow and DYNLAB have relatively close results for the leakage flow. Additionally, it was noted that DYNLAB overestimates the rotordynamic forces within the labyrinth seal when compared to the TASCflow results.

Kirk and Guo [15] most recently used TASCflow and bulk flow to study the influence of leak path geometry and friction on inlet swirl in a labyrinth seal. The TASCflow results show that a diverging leak path will generate larger inlet swirl values than a uniform leak path. Additionally, it was shown that a converging leak path will generate smaller inlet swirl values than a uniform leak path. In general, it was shown that there were significant differences between the TASCflow and bulk flow inlet swirl results. The bulk flow inlet swirl results were shown to vary as much as 149% from the TASCflow results, and provide an overestimated prediction of the inlet swirl velocities when compared to TASCflow.

Section 2: API Seal Introduction

2.1 Purpose of API Study

The American Petroleum Institute (API) is an organization that oversees many aspects of the oil and natural gas industry. One division controls the standards applied to the operation of petroleum and petrochemical equipment [16]. A set of standards managed by the API is the stability specifications of axial and centrifugal compressors. In May 2006, the API sent out a survey to respected bearing and labyrinth seal analysts requesting bearing and labyrinth dynamic coefficients for specified geometries and operating conditions. The resulting study analyzed the variability in responses and also used common titling pad bearing analysis codes to produce and compare bearing coefficients.

2.2 Results of Study

The API survey incorrectly identified the first critical speed of the compressor as 6700 CPM. The correct critical speed is 9700 CPM. This error did not affect the results that used synchronous values for the bearing and labyrinth seal coefficients, but it did have an effect on the non-synchronous values. Overall, the API study concluded that there was wide variation in the coefficients found through different methods. The authors then stated that a new standard for experimental data was needed, so that the experimental data could be used to verify the analytical results and resolve the variability issue.

2.3 Labyrinth Seal Characteristics

This research focuses upon the stage one impeller eye seal characteristics. The given geometry is shown in Figure 2-1 with the dimensional specifications in Table 2-1. The eye seal was specified to be teeth-on-rotor with a pre-swirl at the inlet of 70% of the surface speed. Table 2-2 shows the API specified operating conditions for the stage one impeller eye seal. The working fluid is gaseous nitrogen.

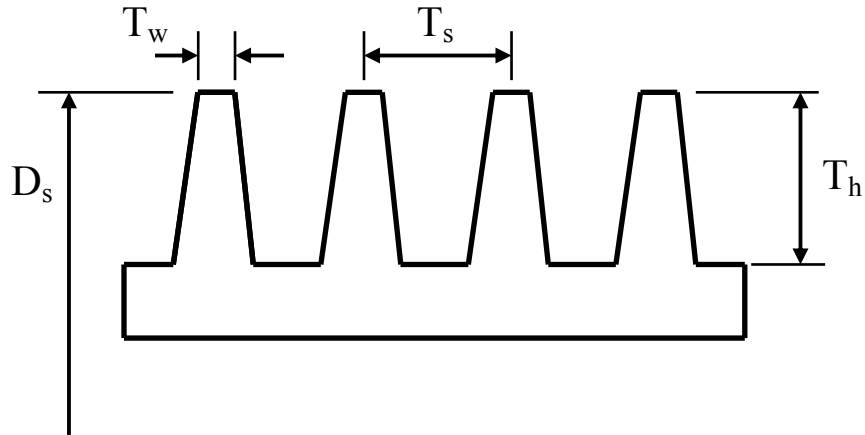


Figure 2-1. API Seal Geometry.

Table 2-1. API Seal Geometric Dimensions.

Dimension	Value
Diameter, D_s	133.35 mm (5.25 in)
Radial Clearance, h	0.127 mm (0.005 in)
Pitch, T_s	2.49 mm (0.098 in)
Height, T_h	2.26 mm (0.089 in)
Tip Width, T_w	0.406 mm (0.016 in)
Number of Teeth	4

Table 2-2. API Seal Operating Conditions.

Condition	Value
Speed	21662 RPM
Discharge Pressure	8.28 MPa (1201 psi)
Inlet Pressure	10.68 MPa (1548 psi)
Discharge Temperature	22.2 °C (72 °F)
Inlet Temperature	52.2 °C (126 °F)
Inlet Swirl	70%
Gas	Nitrogen

2.4 API Seal Modifications

The original API seal was specified to be tooth-on-rotor. Obtaining results with a commercial CFD code for a tooth-on-rotor seal can be difficult, so the seal was changed to the tooth-on-stator configuration. Tooth-on-stator seals are moderately more stable than tooth-on-rotor seals [17, p.

322-3]. Since tooth-on-stator seals are more stable, changing the seal to tooth-on-stator does change the overall dynamic characteristics of the seal. For the intentions of this research, the change is not significant because the CFX tooth-on-stator results are only compared to tooth-on-stator results from other computational programs.

Due to the constraints of ANSYS-CFX, the flow path geometry used to obtain results was modified as shown in Figure 2-2. The modification was required because the API specifications required both an inlet pressure and velocity for the seal, but CFX only allows for the specification of either an inlet pressure or an inlet velocity. The pre-seal section of Figure 2-2 was added so that solely an inlet pressure could be supplied to the pre-seal. Once the flow enters the API seal it has the required inlet pressure and velocity, therefore the pre-seal is a valid workaround for the CFX issue.

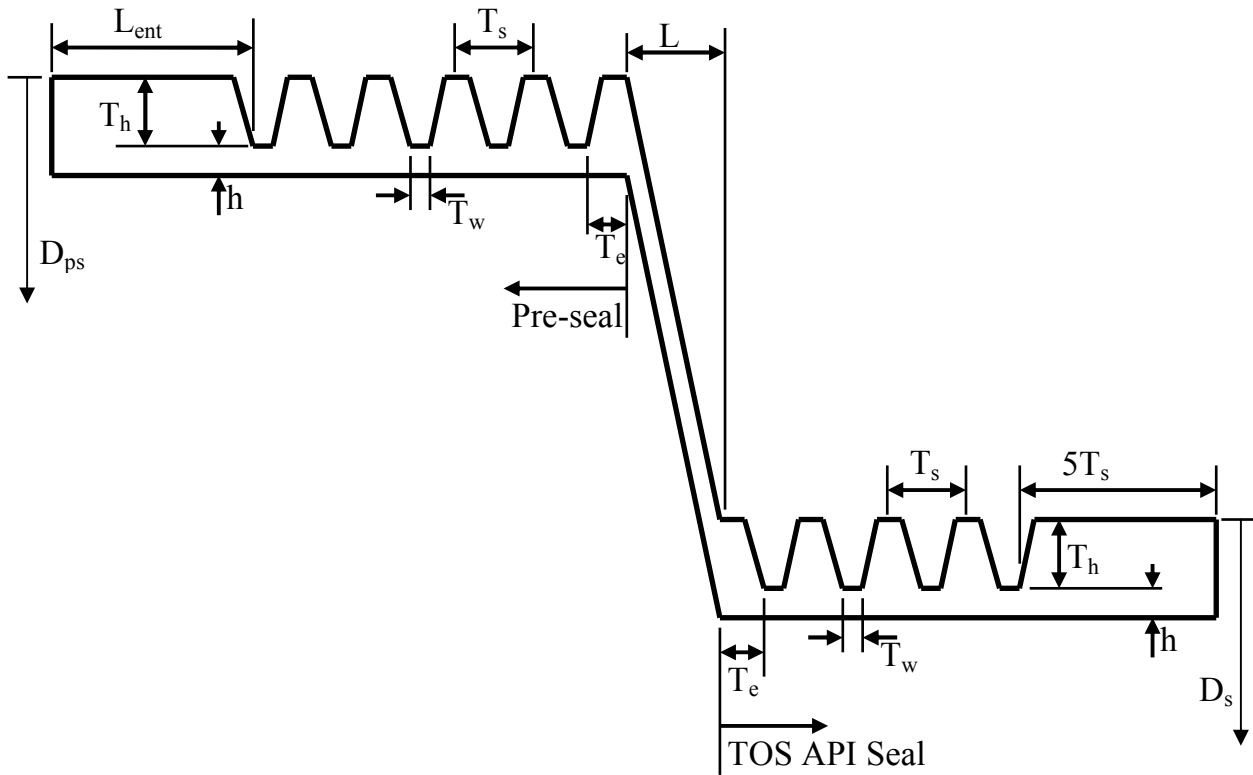


Figure 2-2. Modified API Seal with Added Pre-Seal Flow Path.

Section 3: Tooth-on-Stator Seal Characteristics

3.1 Model

The basic flow path geometric model for this research is shown in Figure 2-2. The pre-seal has the geometric characteristics specified in Table 3-1, while the API seal has the same characteristics given in Table 2-1. As stated before, the pre-seal was added to work around the inlet condition specification issues of CFX. One major drawback of adding the pre-seal is it adds a significant number of nodes to the mesh. Since the academic version of CFX was used for this research, the maximum allowed number of nodes was 250,000. As the flow through the pre-seal is not relevant to this research, the added pre-seal nodes only serve to decrease the number of nodes that can be used in the API seal. If the pre-seal was not necessary, the maximum number of nodes could be used in solely the API seal to increase the mesh resolution and theoretically obtain more precise results.

Table 3-1. Pre-Seal Geometric Characteristics.

Dimension	Value
Diameter, D_{ps}	188.5 mm (7.42 in)
Radial Clearance, h	0.127 mm (0.005 in)
Pitch, T_s	2.49 mm (0.098 in)
Height, T_h	2.26 mm (0.089 in)
Tip Width, T_w	0.406 mm (0.016 in)
Exit Spacing, T_e	2.49 mm (0.098 in)
Entry Length, L_{ent}	12.45 mm (0.49 in)
Horizontal Spacing, L	9.4 mm (0.37 in)
Number of Teeth	5

The operating conditions for the API seal were specified earlier in Table 2-2. The pre-seal inlet conditions were found to be those in Table 3-2. The conditions in Table 3-2 were found by a combination of basic pressure and temperature calculations and trial and error within CFX.

Table 3-2. Pre-Seal Inlet Conditions.

Condition	Value
Inlet Pressure	13.1 MPa (1900 psi)
Inlet Temperature	48.9 °C (120 °F)
Inlet Swirl	0%

Several assumptions were made in this research. The first assumption is the rotor is whirling in the forward direction. The next is that the nitrogen behaves as an ideal gas. The ideal gas assumption is for gases at high temperatures and low pressures, but in this research it was used because the non-ideal gas assumption would be too difficult to implement in CFX. Another assumption is there was a no-slip condition inside of the labyrinth seal. The no-slip condition is a good assumption, because without it, labyrinth seals wouldn't function in the way they were designed. A final assumption is that the walls within in the model are smooth. Wall roughness will have an effect on the flow through the labyrinth seal, but the smooth wall assumption was made because any wall roughness setting would have been an arbitrary guess.

3.2 Mesh

The mesh was created in ANSYS Workbench using the CFX-Mesh option. This option focuses on creating a mesh that has the necessary characteristics for use in a CFD solver. A CFD mesh differs from other solid meshes because it focuses on refining the flow in boundary layer regions and has different element aspect ratio criteria [18].

3.2.1 CFX-Mesh Procedure

CFX-Mesh has many options for creating and refining a mesh. For the meshes created for this research, the commonly used and modified options were: Default Body Spacing, Default Face Spacing, and Face Spacing. The Default Body Spacing applies to all bodies in the model and specifies the maximum element size for the part when no other spacing is specified. The Default Body Spacing was set to be the coarsest desired spacing for the mesh. The Default Face Spacing applies to all faces in the model. It specifies the coarsest face spacing desired in the model. The values of maximum and minimum edge length are specified here, as is the angular resolution of the face elements. The angular resolution is defined by ANSYS to be the “maximum angle allowed to be subtended by the arc between two adjacent surface mesh nodes.” [18] Figure 3-1 is included to provide more clarity to this definition. The nodes are located at the line

intersections and φ is the angular resolution. Face Spacing was also applied in CFX-Mesh. Face Spacing is applied directly to faces where more mesh resolution is desired and supersedes the Default Face Spacing. Face Spacing allows the same mesh variables to be specified as in the Default Face Spacing.

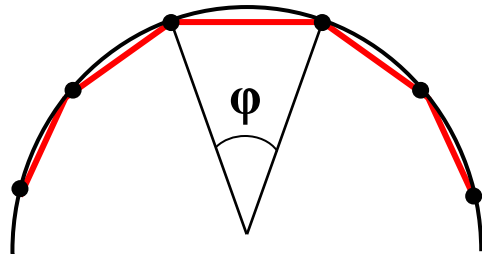


Figure 3-1. Pictorial Representation of Angular Resolution.

3.2.2 CFX-Mesh Advantages and Drawbacks

One of the major advantages to using CFX-Mesh is it simplifies the meshing procedure and allows the mesh to be refined where needed. This reduces the overall time to create the mesh. Another advantage is the graphical user interface (GUI) of CFX-Mesh is relatively easy to use and understand.

There are several drawbacks to the CFX-Mesh program. While it is easy to specify the desired overall mesh characteristics, it can be difficult to refine the mesh in the exact way that the user wants without a significant amount of time spent varying the mesh controls and options. Another drawback is the program only “free-meshes” with tetrahedrons. Overall, it seems that it would have been easier to make a structured mesh to satisfy the desired mesh characteristics in this research. Additionally, it is not desirable that CFX-Mesh only generally states that the created mesh has elements with undesirable aspect ratios. This requires the user to post process the mesh and manually hunt for those elements.

3.3 Pre-Processing

CFX-Pre was used to pre-process the data. The program allows the user to specify all of the flow characteristics for the model. The most important aspect of pre-processing is the rotating reference frame. The model was given a rotating reference frame to convert the transient

solution to a steady-state solution. Additionally, when a rotating frame of reference is specified in CFX, the Coriolis and centrifugal moment terms are included in the solver. In this research, when the rotating reference frame was specified, the portion of the fluid model in direct contact with the stator had to be set to rotate in the opposing direction of the rotating frame. Figure 3-2 shows this concept pictorially.

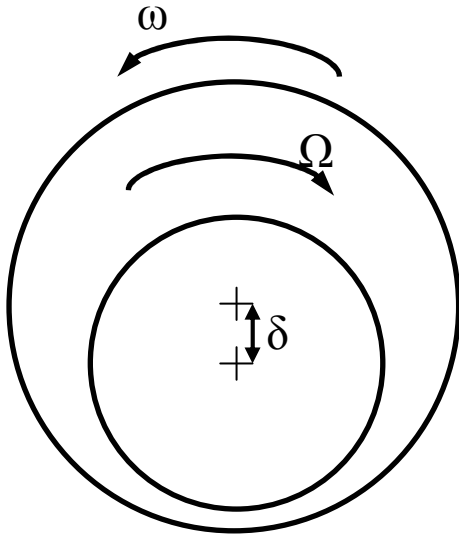


Figure 3-2. Rotating Reference Frame.

3.4 Solution Procedure

There were two different solution procedures followed in this research. The first procedure used four runs at the same whirl speed, each time increasing the number of nodes in the mesh. This allowed the solution to first converge for a smaller number of nodes, then to move on to a larger number of nodes until the desired or maximum number of nodes was reached. This procedure is henceforth named the “Node Increase Method.” The second procedure used two runs. Each run is at the maximum desired number of nodes. The first run is solved with a laminar solution method, and the second run is solved with a turbulent solution method. This procedure has been named the “Laminar/Turbulent Method.”

3.4.1 Node Increase Method

The solution procedure for this method is as follows:

1. Create a mesh in CFX-Mesh.
2. Run this mesh in CFX-Solver until solution convergence.

3. Examine the results to verify the inlet and outlet conditions and confirm there are no problems.
4. Create a finer mesh in CFX-Mesh than the previous mesh.
5. Run the new mesh in CFX-Solver with the results from the previous CFX-Solver run as the initial results until solution convergence.
6. Examine the new results to verify the new inlet and outlet conditions and confirm there are no problems.
7. Repeat Steps 4-6 as necessary.
8. Post-process the final results.

3.4.2 Laminar/Turbulent Method

The solution procedure for this solution is as follows:

1. Create a mesh in CFX-Mesh with the maximum desired number of nodes.
2. Run this mesh with the laminar solution method in CFX-Solver until solution convergence.
3. Run the same mesh as in Step 1 with the turbulent solution method in CFX-Solver using the results from the laminar run as the initial results until solution convergence.
4. Post-process the final results.

3.4.3 Discussion

The Node Increase Method was chosen first because it has quick run times. However, a new mesh had to be created for each run, and this added a significant amount of time to the overall time needed to obtain a solution for each whirl speed. After using the Node Increase Method for some time, it was found that the solution method would not converge for low whirl speeds, so a new procedure had to be established. The Laminar/Turbulent Method was found to work for all whirl speeds above approximately 10% of the running speed (roughly 2200 RPM). This was better than the Node Increase Method, which started having problems below 30% of the running speed.

3.5 Solution Times

The whirl speed study had lower overall solution times because it was converged to the 10^{-4} residual level, while the eccentric study was converged to the 10^{-5} level. There is a discrepancy

because after the whirl speed study, it was determined that the 10^{-5} residual level was preferable, so the next study performed (the eccentric study) used the new residual value. In general, reducing the converged residual level increases the solution time because it takes more iterations to reach a smaller residual.

3.5.1 Whirl Speed Study

On average, 4 meshes were created for each whirl speed run. Table A-1 in Appendix A contains the number of nodes, runtimes, and iterations for each run of all the whirl speeds. The total average run time was approximately 3 hours and 10 minutes, using a 2.4 GHz processor. There was a great deal of variation in the total run time of each whirl speed run. In general, as the whirl speed decreased, the time to reach a solution increased. This is illustrated in Figure 3-3. The 100, 86.33, 75, 60, 50, and 25 percent cases were run with the Node Increase procedure, while the 30 and 15 percent cases were run with the Laminar/Turbulent procedure. As stated before, the Laminar/Turbulent Method increased the solution time, but produces converged solutions that the Node Increase Method could not converge.

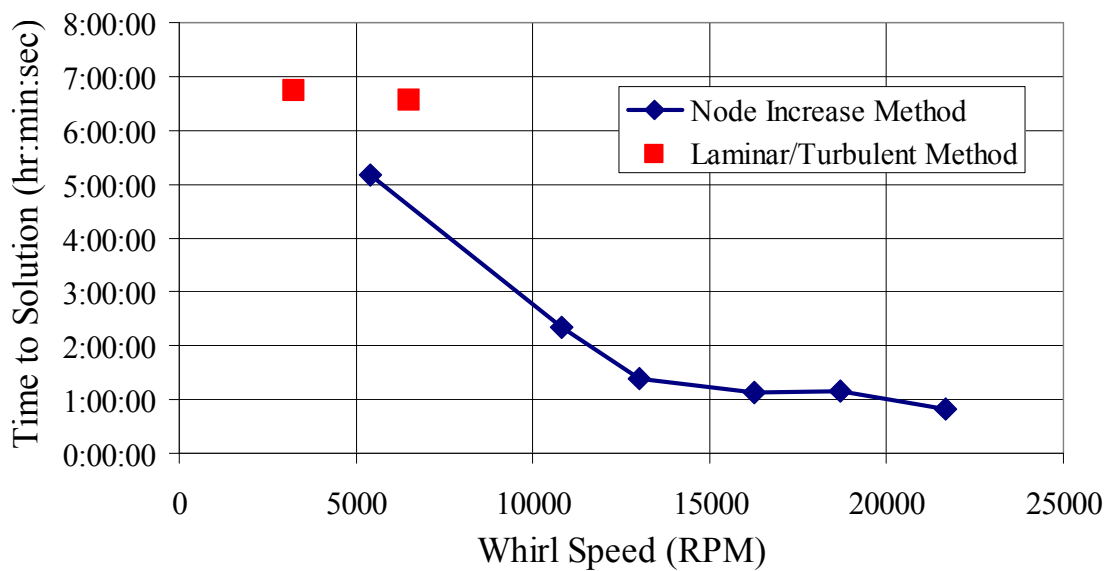


Figure 3-3. Whirl Speed Versus Time to Solution for the Whirl Speed Study.

3.5.2 Eccentric Study

One mesh was created for each eccentricity study, and was used for both the laminar and turbulent runs. Table A-2 in Appendix A contains the number of nodes, runtimes, and iterations for each of the eccentricities. The total average run time was approximately 6 hours and 40 minutes, again using a 2.4 GHz processor. With the exception of the 0.1 eccentricity ratio case, increasing the eccentricity ratio increased the time to converge to a solution. Figure 3-4 shows the time to converge to a solution for each case.

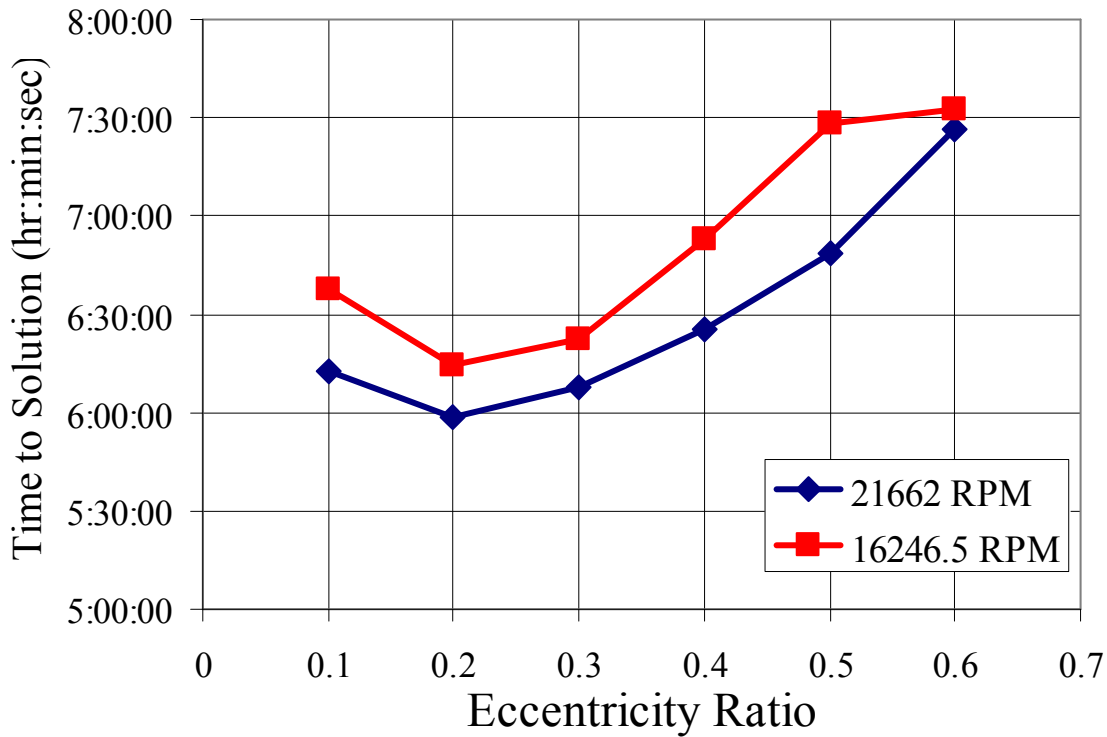


Figure 3-4. Eccentricity Ratio Versus Time to Solution for the Eccentric Study.

3.6 Post Processing

The data was post processed using CFX-Post and Microsoft Excel. CFX-Post was used to create objects such as pressure contours, velocity vectors, and streamlines. CFX-Post also has the capability to export data for many different flow variables. The exported file was viewed and manipulated in Excel to obtain many of the values in this research such as forces, average pressures, and various plots. One advantage to CFX-Post is that it is relatively easy to use and

export data. Conversely, one disadvantage to CFX-Post is it does not have enough options for displaying and exporting the data in a way that is applicable to this research. A disadvantage of using Excel to process the CFX-Post exported data is at times the numbers of rows of data in the exported file exceed the maximum number of rows available in an Excel worksheet. This means some time has to be spent to break up the exported file into a manageable size that Excel will accept.

Section 4: Whirl Speed Variation Within ANSYS-CFX

4.1 Purpose

The whirl speed study was conducted to compare the results of CFX to the results of other programs. The CFX results will be compared to ANSYS-TASCflow, a bulk flow code (VT-FAST), and LabyXL. TASCflow is a CFD code that has since been superseded by ANSYS-CFX and has also been used by the Virginia Tech Rotor Dynamics Lab to model the flow through labyrinth seals [13-15].

4.2 Results

The flow path geometry from Figure 2-2 was used here with an eccentricity ratio of 0.1 for all of the whirl speeds. The created model is shown in Figure 4-1, with a cutaway view in Figure 4-2. The target flow conditions are given in Table 2-2. An inlet swirl of 70% is rather high for a labyrinth seal and fairly difficult to reach in CFX. High inlet swirl values are hard to achieve in CFX because it is difficult to have a large portion of the flow in the circumferential direction due to the no-slip condition along the stator. For this study, an inlet swirl value of 62.6% was obtained for all whirl speeds. In comparison, the TASCflow results are for 62% inlet swirl, and the bulk flow code results are for 64% inlet swirl. The CFX inlet swirl falls within the range of the swirl in the TASCflow and bulk flow cases. The inlet pressure varied for each whirl speed, but the maximum percent difference between the desired inlet pressure of 10.68 MPa (1548 psi) and the actual inlet pressure was only 1.7%. The inlet pressure for each whirl speed with relation to the desired inlet pressure is given in Figure 4-3. Figure 4-4 shows how the percent difference of the actual inlet pressure from the target inlet pressure varies with whirl speed.

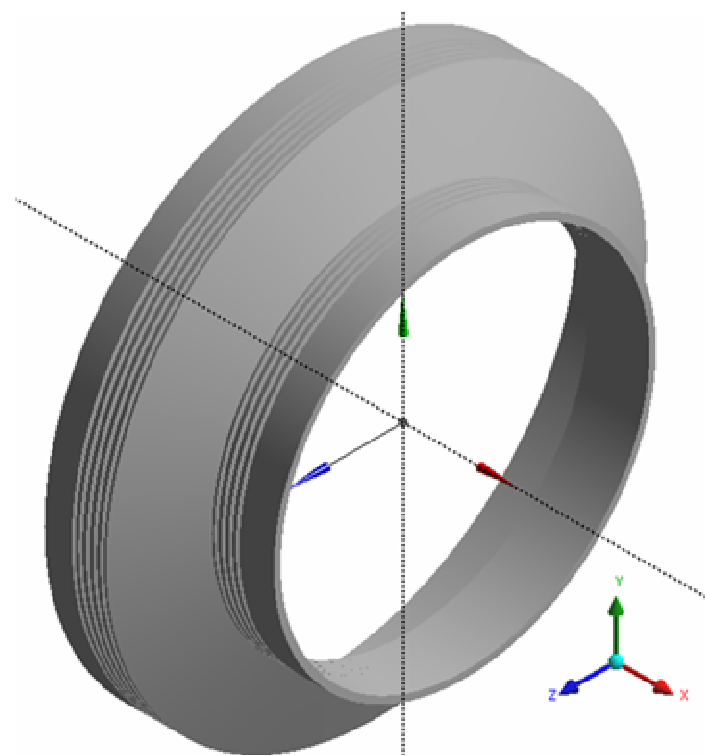


Figure 4-1. Full Whirl Speed Study Flow Path.

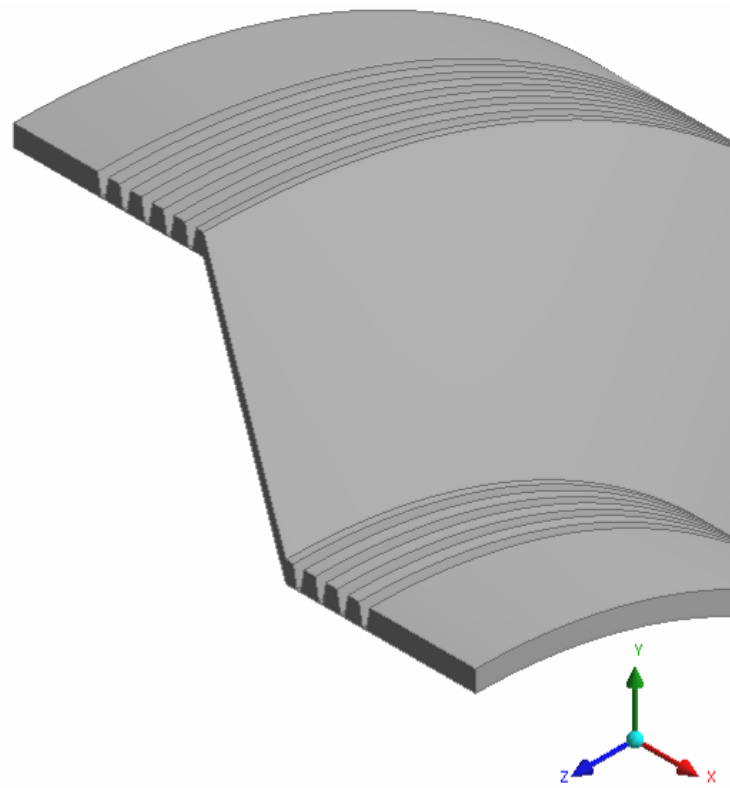


Figure 4-2. Whirl Speed Study Flow Path Cutaway.



Figure 4-3. Inlet Pressure Versus Whirl Speed.

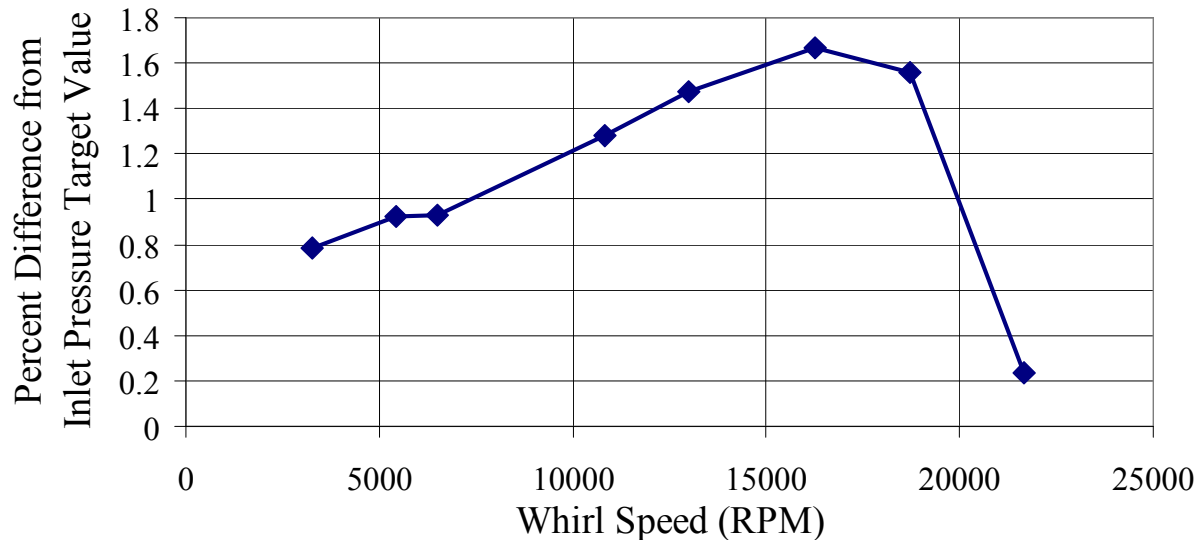


Figure 4-4. Percent Difference from Inlet Pressure Target Value Versus Whirl Speed.

Appendix B contains representations of the flow through the seal for the 21662 RPM case. Figure B-1 shows the pressure distribution in the seal. Figure B-2 shows a close-up view of the pressure distribution in the API seal. It can be seen that there is a drop in pressure between each labyrinth cavity. Figure B-3 shows the stationary frame velocity contours for the API seal. The

velocity contours show the flow is moving at the running speed along the rotor, and is zero along the stationary walls. This is the expected flow pattern for the labyrinth seal. Figure B-4 contains the stationary frame velocity vectors for the API seal. The velocity vectors show the same information as the velocity contours, but in three-dimensional space. Finally, Figure B-5 shows the stationary frame velocity 2-D streamlines for the chamber between the second and third teeth in the API seal. Figure B-5 illustrates, as expected, the circulation within the labyrinth seal chambers.

There are two elements of the tangential force acting upon the rotor: shear forces and forces due to a circumferential pressure distribution. It has been shown in previous work [7] that the shear component of the tangential force accounts for one percent of the total tangential force. For this reason, the shear component of the tangential force can be neglected.

The forces on the rotor were calculated from data exported from CFX-Post. The geometry was aligned so that the x-direction is axial, the y-direction is radial, and the z-direction is tangential. The force components are found as in Equation 4-1:

$$\begin{aligned} F_x &= P * A_x \\ F_y &= P * A_y \\ F_z &= P * A_z \end{aligned} \quad (4-1)$$

The components of A are shown in Equation 4-2:

$$\begin{aligned} A_x &= A * n_x \\ A_y &= A * n_y \\ A_z &= A * n_z \end{aligned} \quad (4-2)$$

The calculated forces are the forces acting on the surface of the rotor due to the CFX calculated pressure. A positive tangential force indicates a force in the direction of the whirl, while a positive radial force indicates a restoring force opposite the direction of the rotor offset. Figure 4-5 shows this concept pictorially. The sign on the forces calculated from the CFX exported data had to be switched because the solution was run in a rotating reference frame. When switching

to a stationary reference frame, the flow changes direction relative to the stationary coordinate system. This change in direction causes the forces created by the flow to also change direction when viewed in a stationary frame.

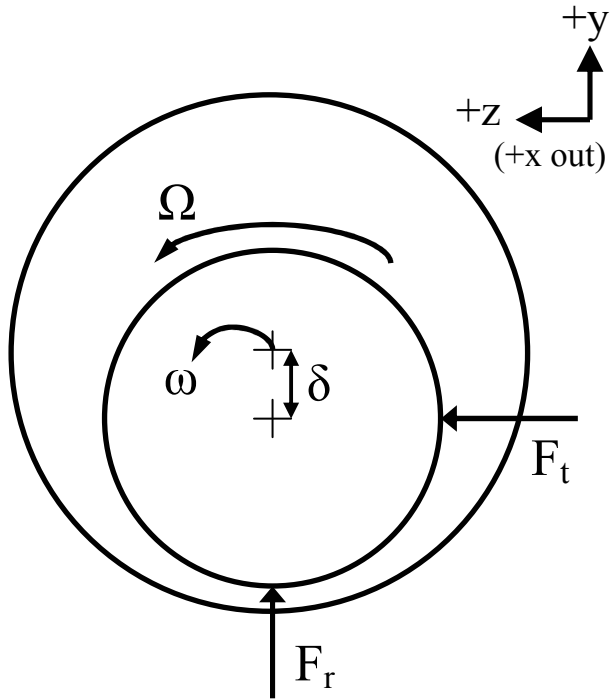


Figure 4-5. Rotor Force Representation.

The calculated radial forces for all whirl speeds are in Figure 4-6. Except for the 21662 RPM whirl speed case, the magnitude of the radial force on the rotor increases with decreasing whirl speed. The same trend is observed with the tangential force, as illustrated in Figure 4-7. In the non-synchronous whirl cases, the negative value of the radial force shows that the seal is pushing itself towards larger eccentricities. However, the seal has a restoring force component in the synchronous whirl case. The positive tangential force components for both the synchronous and non-synchronous whirl are consistent with the assumption of forward whirl of the rotor.

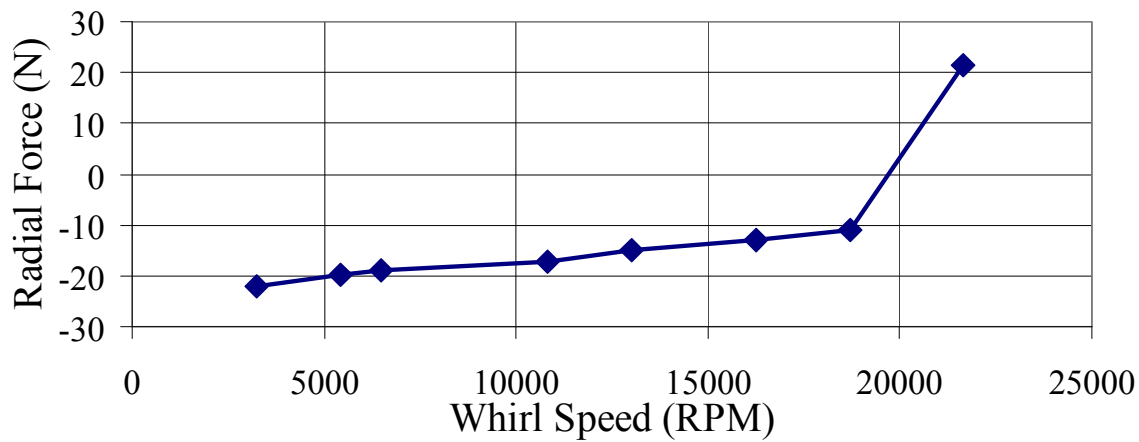


Figure 4-6. Radial Force on the Rotor Versus Whirl Speed.

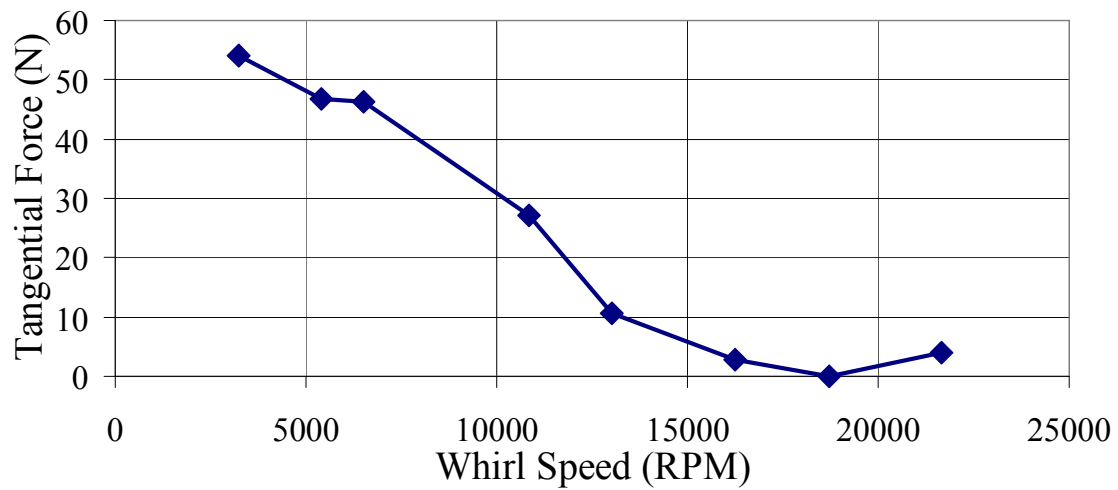


Figure 4-7. Tangential Force on the Rotor Versus Whirl Speed.

The stiffness and damping coefficients for the seal were also computed for each whirl speed. Equations 4-3 and 4-4 are used to determine the coefficients:

$$\frac{F_r}{\delta} = -K - \Omega c \quad (4-3)$$

$$\frac{F_t}{\delta} = k - \Omega C \quad (4-4)$$

As was stated earlier, the y -direction corresponds to the radial direction and the z -direction corresponds to the tangential direction. Table 4-1 contains the dynamic coefficients for the seal. Another seal characteristic is the effective cross-coupled stiffness, Q_e , as shown in Equation 4-5:

$$Q_e = k - C\omega_{Ncr} \quad (4-5)$$

Table 4-1. Dynamic Coefficients.

C (N-s/m)	k (N/m)	c (N-s/m)	K (N/m)	Q _e (N/m)
-1.755E+02	-7.527E+04	-4.803E+03	9.195E+06	1.984E+05

4.3 Comparison of CFX Results to Bulk Flow and TASCflow Results

The CFX force results were compared with those from bulk flow and TASCflow. The forces from each result were divided by the eccentricity (δ), so the data could be easily compared. Figure 4-8 shows the radial results for CFX, TASCflow, and the bulk flow code. Figure 4-9 shows the tangential results for all three solution methods. TASCflow results were only available for the following whirl speeds: 0 RPM, 5415.5 RPM, and 10831 RPM. TASCflow was unable to converge solutions for whirl speeds above 10831 RPM, so no TASCflow data is available past 10831 RPM. CFX did not have problems converging solutions at higher whirl speeds, but had difficulty converging solutions below 5415.5 RPM.

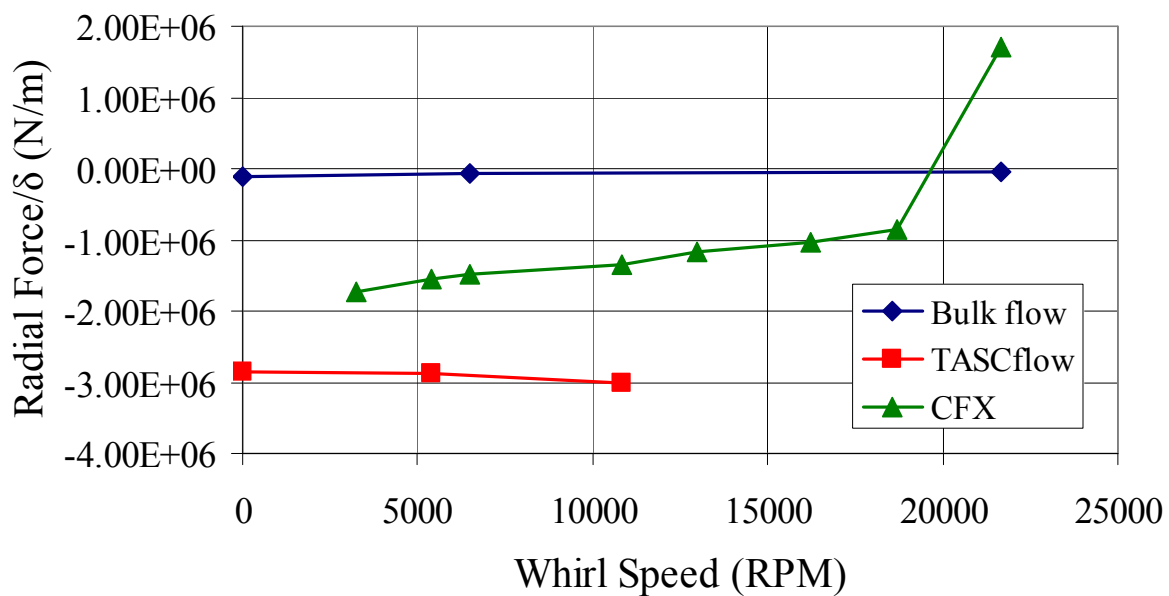


Figure 4-8. Radial Force/ δ Versus Whirl Speed.

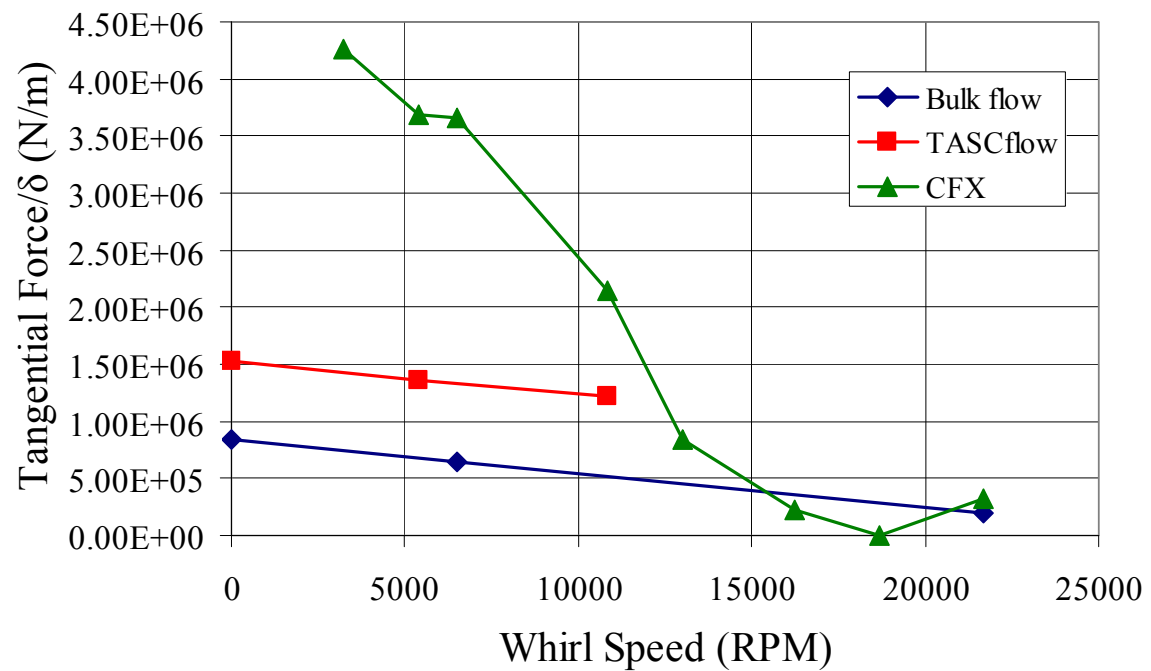


Figure 4-9. Tangential Force/ δ Versus Whirl Speed.

It can be seen that the CFX results begin to come close to the bulk flow results at higher whirl speeds, especially when examining the tangential forces. In general, there are large discrepancies among the results for the three cases. Several hypotheses have been formulated to explain the discrepancies.

Previously, the bulk flow code produced forces that were more destabilizing than the CFD computed results [13-15]. The previous work used lower inlet swirl values than used in this research. The inlet swirl discrepancy is a possible reason why the CFD programs now produce the most destabilizing results.

One possible explanation for the discrepancy between CFX and TASCflow is the presence of large differences between the CFX mesh and the TASCflow mesh. First, the CFX mesh is considered a “free mesh”, while the TASCflow mesh is a structured mesh. In addition, there was a limitation on the number of nodes in CFX, while the TASCflow mesh could be created with any desired number of nodes. Also, the original mesh density sensitivity study performed in TASCflow [14] was solved at zero inlet swirl. Since the TASCflow results here were solved at 63% inlet swirl, the original mesh density sensitivity study results could be invalid for high swirl values. Furthermore, it was not possible to perform a mesh-sensitivity study in CFX because of the limitations of the CFX software, so it is possible that the CFX results are highly influenced by the mesh.

4.4 Comparison of CFX Results to LabyXL Results

The API seal was analyzed in LabyXL [11]. The original tooth-on-rotor configuration was used so that direct comparisons to the API survey results [12] could be performed. Since the data presented in this research is for tooth-on-stator configurations, it is not possible to directly compare the data. As shown in Table 4-1, the effective stiffness found by CFX is approximately 198,401 N/m. The effective stiffness found from LabyXL is approximately 380900 N/m, which is about 47.9% different from the CFX effective stiffness value.

Section 5: Eccentricity Variation Within ANSYS-CFX

5.1 Purpose

In eccentric seals, the non-uniform pressure distribution along the circumference of the seal causes forces in the seal. The tangential force is thought to have the most destabilizing effect on the seal. Benckert and Wachter [2] discuss this effect and show that the tangential force has a linear relationship with eccentricity up until a critical eccentricity ratio. Overall, the eccentricity variation study was performed to show that the forces in a labyrinth seal increase linearly with increasing eccentricity.

5.2 Results

The flow path geometry of Figure 2-2 was used here with varying values for ε , the eccentricity ratio. The eccentricity ratio is a non-dimensional term and is defined as the eccentricity (δ) divided by the radial clearance (h) of the seal. The model used is in Figure 5-1, with a cutaway of the model shown in Figure 5-2. The target flow conditions are in Table 2-2. The target inlet pressure was again 10.67 MPa (1548 psi). Figure 5-3 shows the actual inlet pressure for each case, while Figure 5-4 shows the percent deviation of each value from the target. The maximum absolute value of the percent deviation is approximately 2.3%.

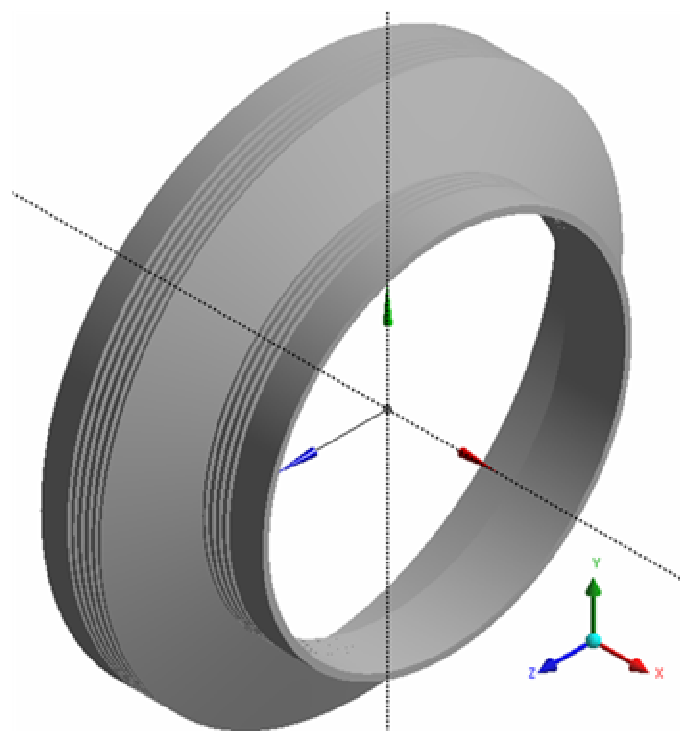


Figure 5-1. Full Eccentric Study Flow Path.

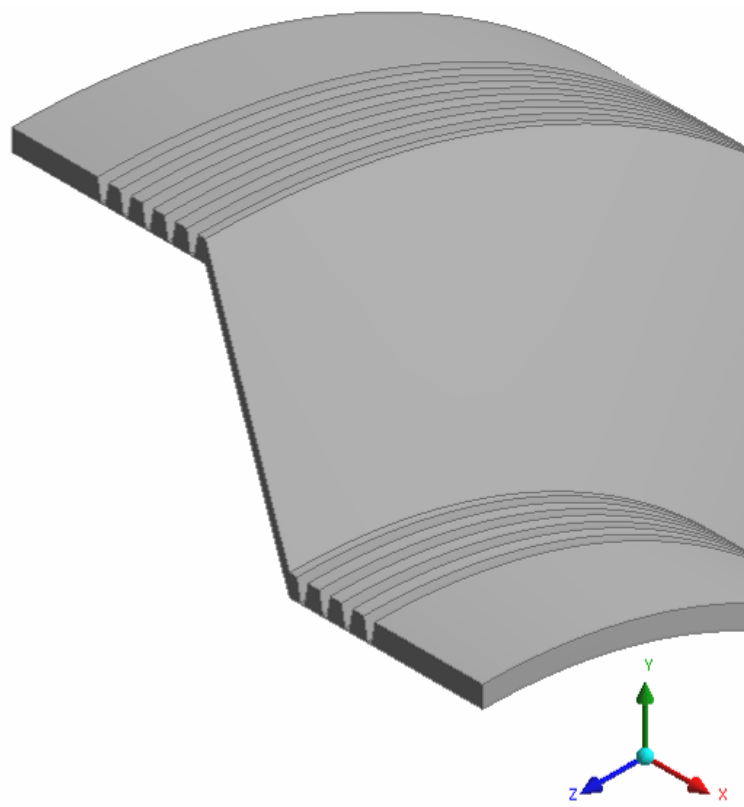


Figure 5-2. Eccentric Study Flow Path Cutaway.

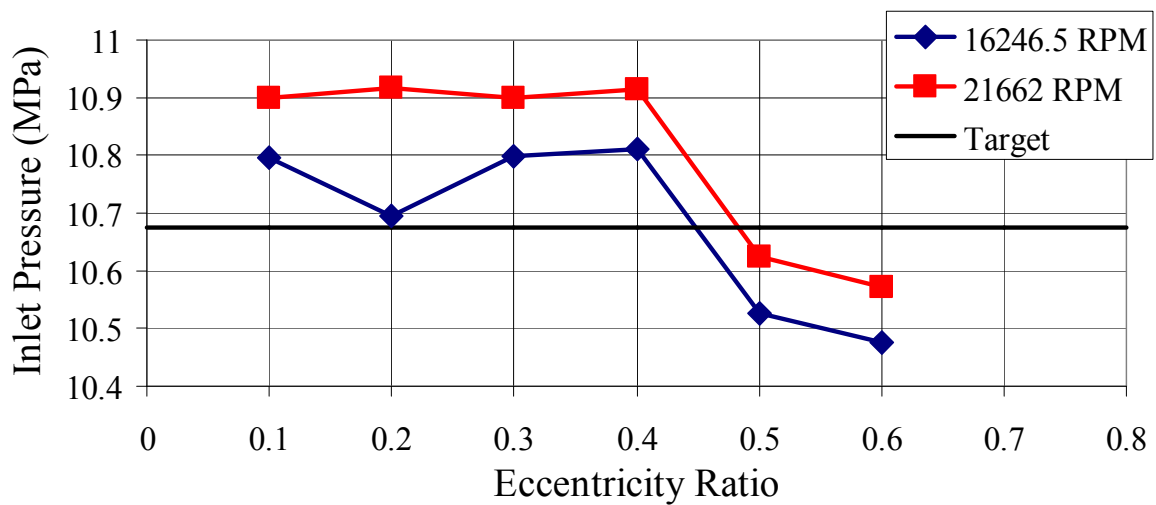


Figure 5-3. Actual Inlet Pressure Versus Eccentricity Ratio.

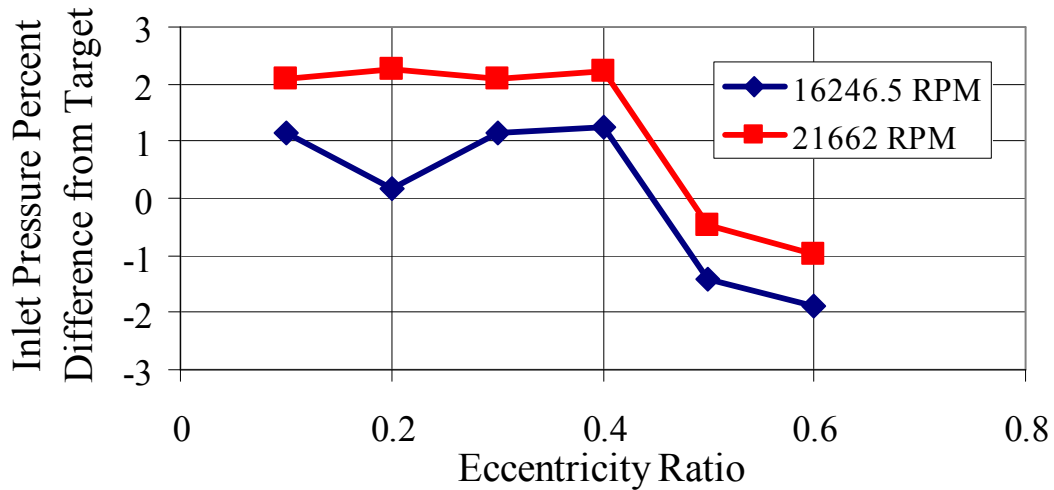


Figure 5-4. Inlet Pressure Percent Difference from Target Versus Eccentricity Ratio.

Appendix C details the flow through the labyrinth seal for the 0.3 eccentricity ratio case at 21662 RPM. The pressure distribution of the entire model is shown in Figure C-1. Figure C-2 shows a more detailed representation of the pressure distribution in the API seal. It is shown that each labyrinth tooth creates a pressure drop. The stationary frame velocity contours are shown in Figure C-3. It is demonstrated that the flow velocity is zero along the stationary walls, and that the flow is moving at the running speed along the rotor. Figure C-4 contains the stationary frame

velocity vectors. The velocity vectors are useful to help illustrate the flow characteristics within the seal. Figure C-5 displays the stationary frame velocity streamlines between the third and fourth teeth. These streamlines show the expected flow circulation within the cavity.

The target inlet swirl was again 70% for all cases. The actual inlet swirl values for each eccentricity value are shown in Figure 5-5. The inlet swirl was the same for each speed run at the each eccentricity. The maximum inlet swirl was 62.92%, while the minimum was 62.36%.

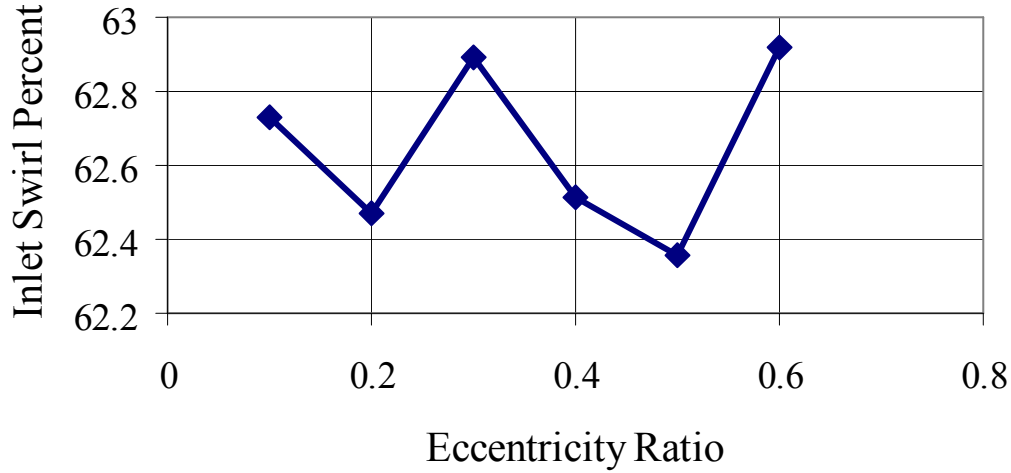


Figure 5-5. Percent Inlet Swirl Versus Eccentricity Ratio.

The circumferential pressure distribution for the 0.3 eccentricity ratio case at 21662 RPM was plotted for the seal in Figure 5-6. There is scatter in the data caused by the uneven mesh, but a fourth order polynomial was fit to the data to show the overall pressure distribution trend. The uneven mesh could not be avoided due to the limitations of CFX-Mesh. The same circumferential pressure distribution was shown in the work of Rajakumar and Sisto [4]. Additionally, the circumferential velocity distribution for the same case is shown in Figure 5-7. The uneven circumferential pressure distribution contributes to the forces in the seal.

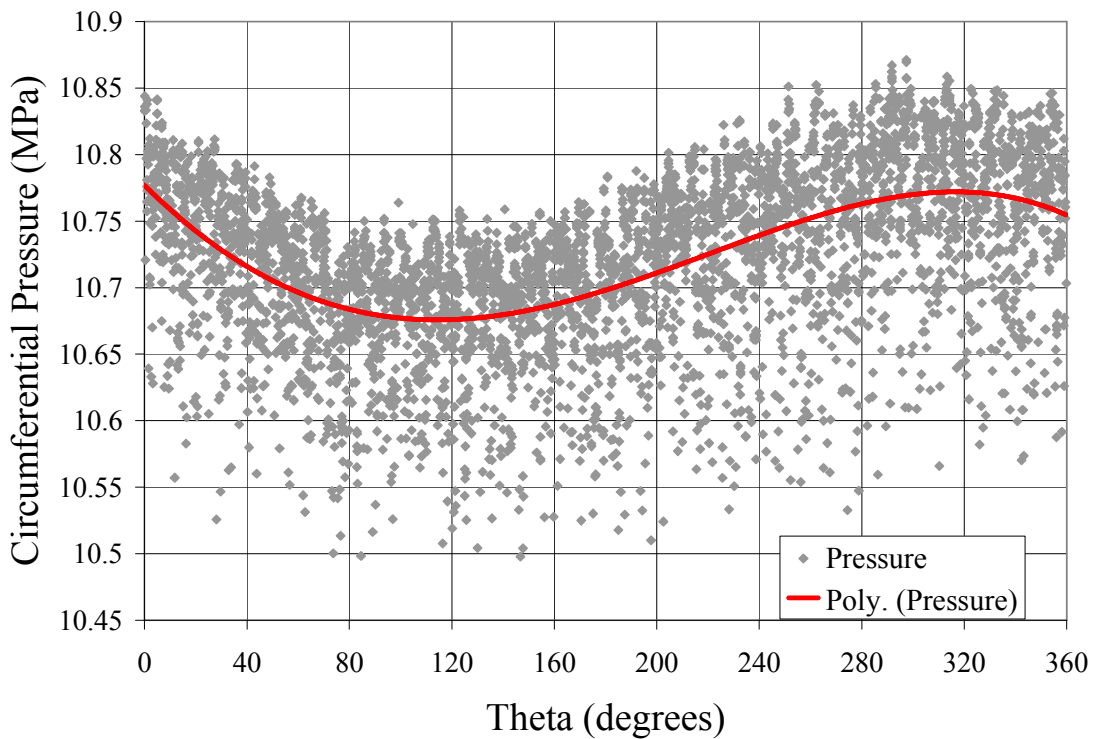


Figure 5-6. Circumferential Pressure Versus Theta.

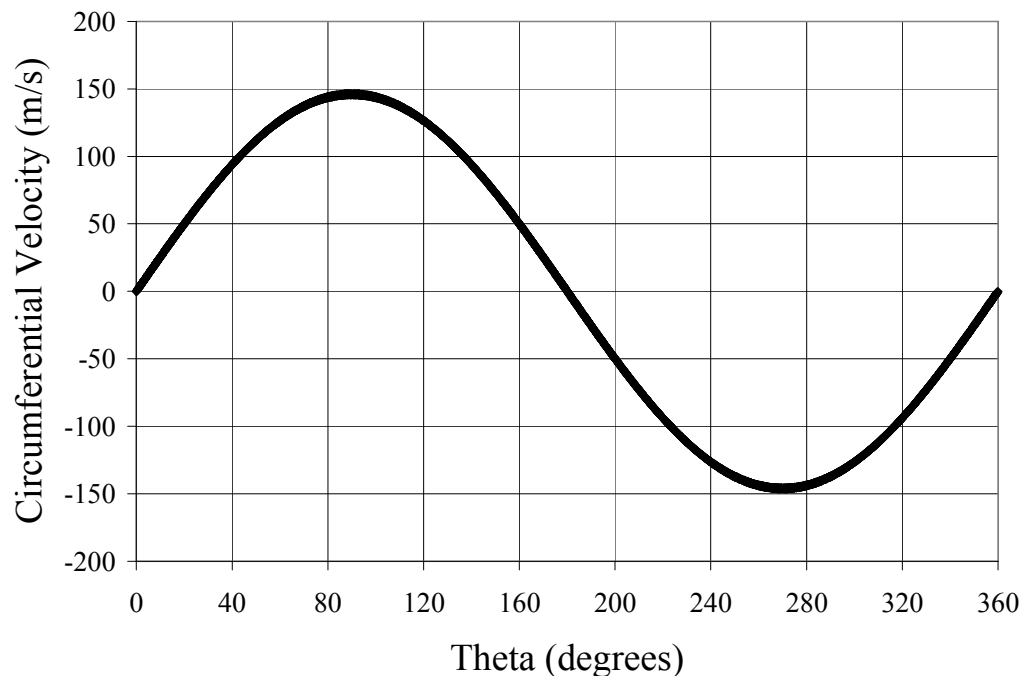


Figure 5-7. Circumferential Velocity Versus Theta.

The forces on the rotor were calculated from the data exported from CFX-Post. The same force calculation procedure from Section 4.2 was followed here. The radial forces shown in Figure 5-8 follow the expected linear trend up until an eccentricity ratio of 0.5 is reached. A good indicator of the linearity of a set of points is the R^2 value of linear fit line. An R^2 value of one indicates that the data is perfectly linear, while an R^2 value of zero signifies no linear relationship. The radial force R^2 value for the 16246.5 RPM case was 0.9875, while the R^2 value for the 21662 RPM case was 0.9929. These very high R^2 values indicate a strong linear relationship between the eccentricity ratio and the radial force for eccentricity ratio values of 0.1 to 0.4.

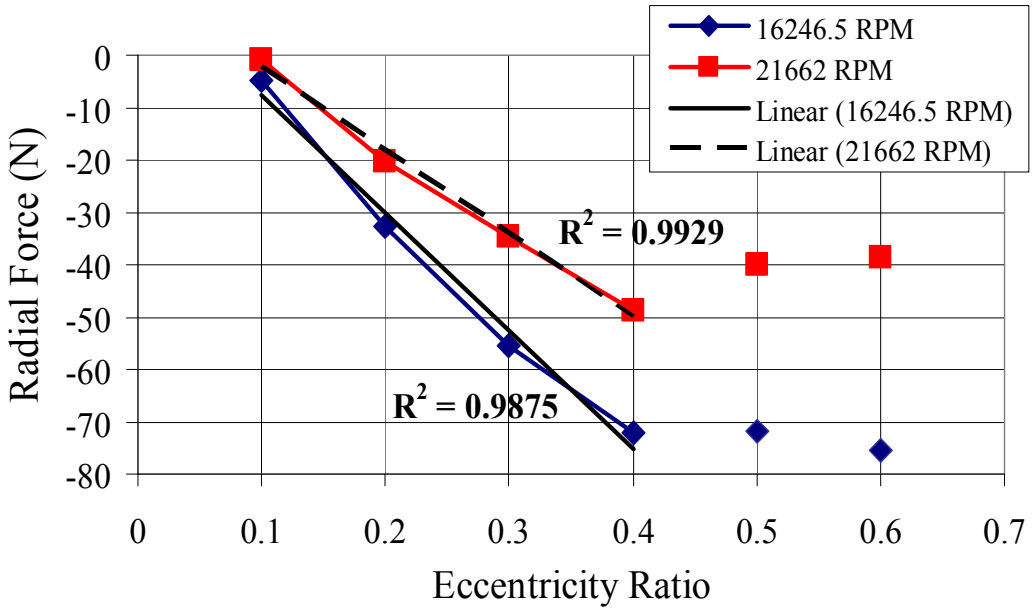


Figure 5-8. Radial Force Versus Eccentricity Ratio.

The trend of the tangential force with respect to the eccentricity ratio was also examined. It was found that the tangential force does not vary linearly with respect to the eccentricity ratio, as seen in Figure 5-9. One possible explanation for this observation is given in Section 5.3.

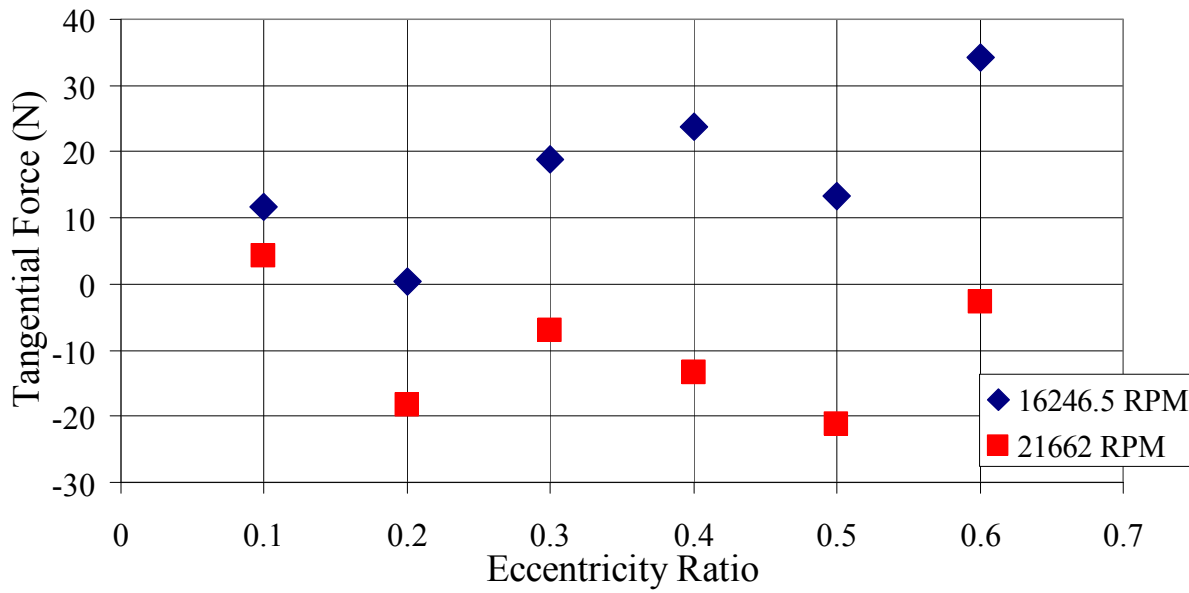


Figure 5-9. Tangential Force Versus Eccentricity Ratio.

The relationships between the eccentricity ratio and the direct stiffness and the cross-coupled stiffness are shown in Figure 5-10 and 5-11 respectively. Figures 5-12 and 5-13 show the relationships between the eccentricity ratio and the direct damping and the cross-coupled damping respectively. The damping and stiffness values were calculated using Equations 4-3 and 4-4. There does not appear to be a relationship among any of the dynamic coefficients and the eccentricity ratio. The effective stiffness was also found using Equation 4-5. Table 5-1 summarizes the dynamic coefficients for the eccentricity ratio study.

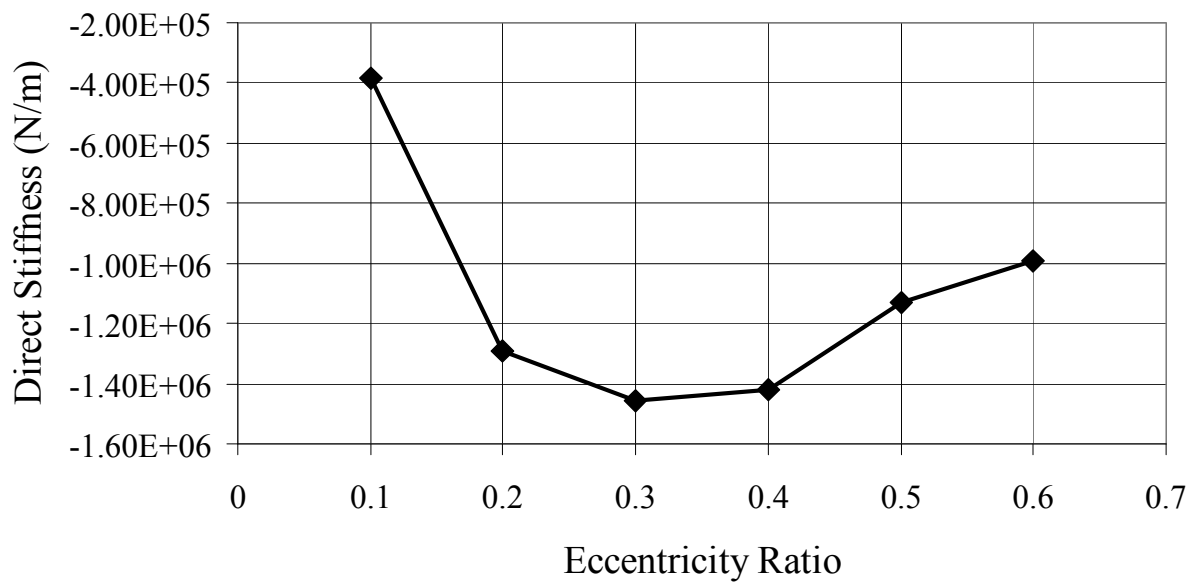


Figure 5-10. Direct Stiffness Versus Eccentricity Ratio.

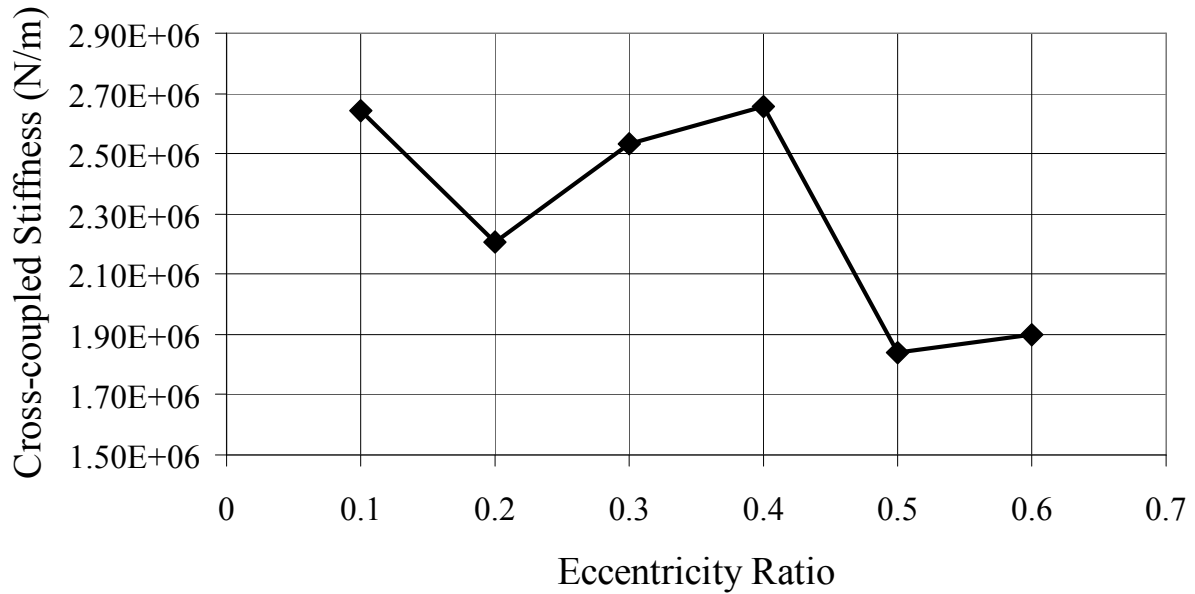


Figure 5-11. Cross-coupled Stiffness Versus Eccentricity Ratio.

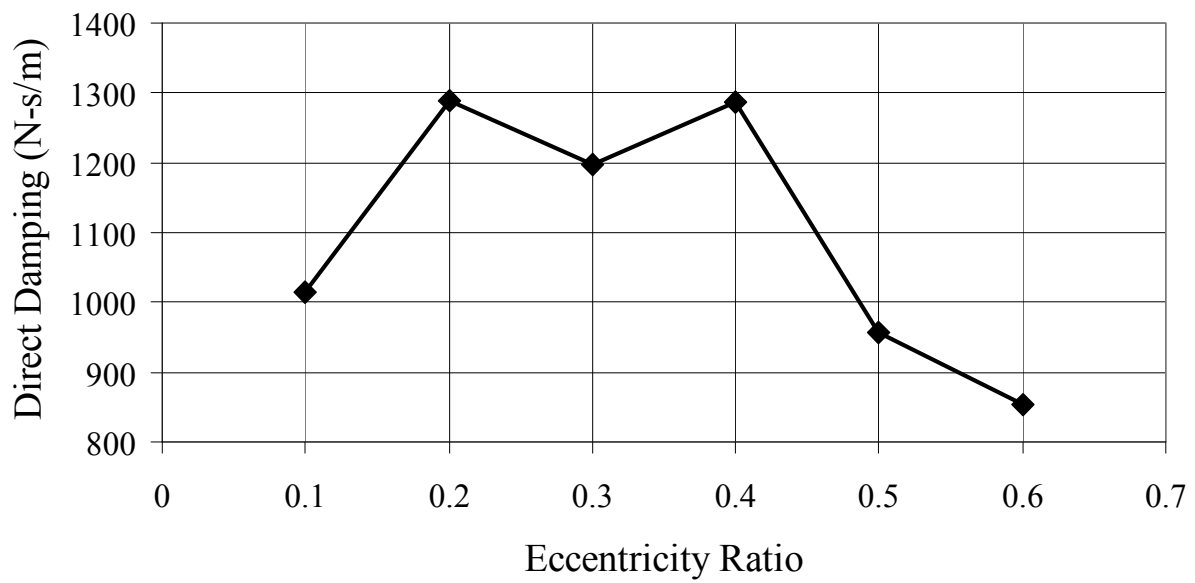


Figure 5-12. Direct Damping Versus Eccentricity Ratio.

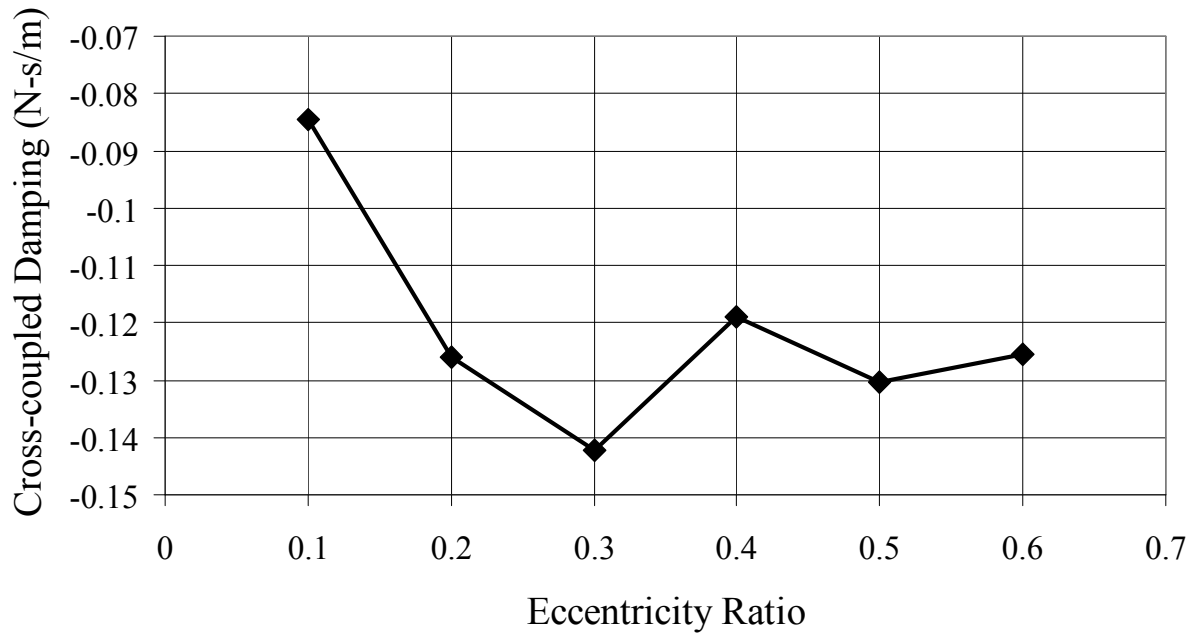


Figure 5-13. Cross-coupled Damping Versus Eccentricity Ratio.

Table 5-1. Dynamic Coefficients for Varying Eccentricity Ratios.

Eccentricity Ratio	Direct Stiffness (N/m)	Cross-coupled Stiffness (N/m)	Direct Damping (N-s/m)	Cross-Coupled Damping (N-s/m)	Effective Stiffness (N/m)
0.1	-3.821E+05	2.643E+06	1.015E+03	-8.457E-02	1.931E+06
0.2	-1.290E+06	2.207E+06	1.290E+03	-1.260E-01	2.207E+06
0.3	-1.459E+06	2.531E+06	1.198E+03	-1.422E-01	2.531E+06
0.4	-1.422E+06	2.658E+06	1.287E+03	-1.191E-01	2.658E+06
0.5	-1.131E+06	1.839E+06	9.577E+02	-1.303E-01	1.839E+06
0.6	-9.902E+05	1.902E+06	8.536E+02	-1.254E-01	1.902E+06

5.3 Comparison to Published Data

Benckert and Wachter [2] discussed the relationship between tangential forces and the circumferential velocity in the labyrinth seal. They noted that the tangential forces are “induced by the circumferential velocity components of the flow in the whirling chambers” [2, p. 193]. They determined that there are two causes for circumferential flow. Drag effects of the shaft are the first cause, and the other cause of circumferential flow is entry swirl. Both of these conditions are accounted for in this research. In Section 3.1, it was discussed that the no-slip condition was assumed in the model. This is analogous to the “drag effects” of Benckert and Wachter’s paper [2]. Additionally, it was assumed that there was inlet swirl in the seal, as also stated in Section 3.1.

Benckert and Wachter also noted that while drag effects dominate the existence of circumferential velocity in longer labyrinth seals, the inlet swirl component dominates the existence of circumferential velocity in short labyrinth seals. They defined short labyrinth as those having five or less spaces between sealing strips. This is analogous to five or less chambers between the teeth in the labyrinth. The short labyrinth condition corresponds to this research.

The correlation between the normalized tangential forces for the 21662 RPM case and the inverse of the normalized inlet swirl is shown in Figure 5-14. The force and swirl values were normalized by dividing the original values by the maximum respective values. Figure 5-14

suggests that there is a relationship between the tangential force values for the 21662 RPM case and the inlet swirl. Since:

1. the labyrinth seal studied here is considered to be a short seal,
2. the short seal circumferential velocity is deemed to be dominated by the inlet swirl, and
3. the tangential forces are induced by the circumferential velocity,

it can be concluded that the change in the inlet swirl for each eccentricity could have caused the variation in the tangential velocity. This conclusion would explain why the tangential forces do not behave linearly with respect to the eccentricity ratio. The 16246.5 RPM case is not considered here because no inlet swirl and tangential velocity correlations for non-synchronous whirl speeds were explicitly found in published papers.

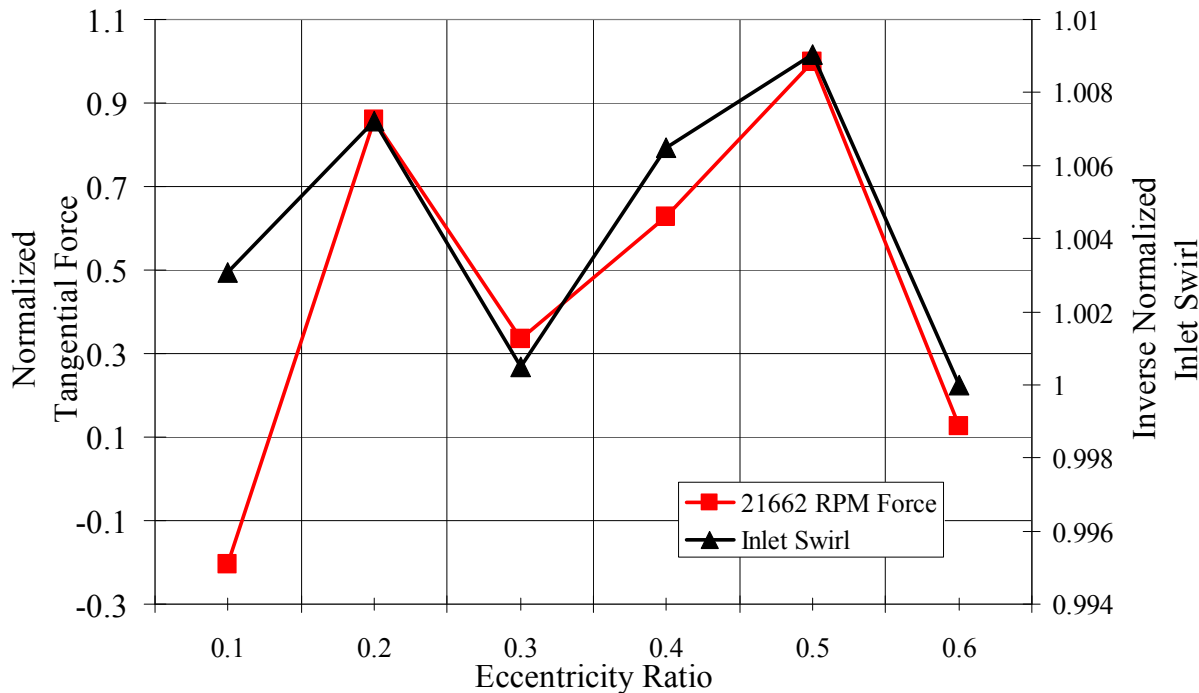


Figure 5-14. Variation of Normalized Tangential Force and the Inverse Normalized Inlet Swirl With Respect to Eccentricity Ratio.

It should also be noted that the relationship between tangential force and inlet swirl could be a result of the mesh used. Since a result independent mesh could not be created, it is not possible to fully know whether or not the relationship shown in Figure 5-14 is physical or due to the mesh

used. As stated before, a result independent mesh could not be created due to the limitations of ANSYS-CFX and CFX-Mesh.

Since the radial force does not result from the circumferential velocity, it is not affected by the variation in inlet swirl. Benckert and Wachter note that the linearity of the radial force with respect to the eccentricity ratio is generally valid for eccentricity ratio values less than 0.4 for the seals they studied. This is validated in Figure 5-8 because the linear relationship ends after the 0.4 eccentricity ratio case. The radial force and eccentricity ratio linear relationship is also verified by Rajakumar and Sisto [4].

Section 6: Summary and Conclusion

6.1 Whirl Speed Study

The relationship between the labyrinth whirl speed and the forces produced was studied. Eight cases were produced with ANSYS-CFX for whirl speeds varying from 15% to 100% of the running speed, with a running speed of 21662 RPM. There were small variations of the inlet pressure, with the largest deviation being 1.7% from the desired inlet pressure of 10.67MPa (1548 psi). The percent inlet swirl was constant for all the cases at 62.6%. It was found that, with the exception of the running speed case, the magnitude of the radial and tangential forces increased with decreasing whirl speeds. This indicates that in the non-synchronous whirl cases, the radial force is pushing the rotor towards larger eccentricities. Both the synchronous and non-synchronous whirl cases have forward whirl. The dynamic coefficients of the seal were found to be those shown in Table 6-1.

Table 6-1. CFX Dynamic Coefficients.

C (N·s/m)	k (N/m)	c (N·s/m)	K (N/m)	Q _e (N/m)
-1.755E+02	-7.527E+04	-4.803E+03	9.195E+06	1.984E+05

The data produced by CFX was compared to data produced by TASCflow and VT-FAST (a bulk flow code). It was shown that there were large discrepancies among most of the force results. At whirl speeds approaching the running speed, CFX and the bulk flow code had the closest agreement. It was shown that the bulk flow code underestimated the results. This is contrary to previous work [13-15], where the bulk flow code overestimated the force results. It was hypothesized that the discrepancy may come from the use of high swirl values, which had not been compared before.

CFX was also compared to TASCflow, another CFD software. It was shown that there was not agreement between the results from each code. It was speculated that there may be several reasons for the discrepancy, all of which stem from the meshes used. Discrepancies may have arisen due to the CFX-Mesh limitations. CFX-Mesh limits the user to a free-mesh and 250,000 nodes, which severely limits the accuracy of the results. The TASCflow results used a mapped mesh, and did not have a software imposed node limit. Additionally, a sensitivity study of the

TASCflow mapped mesh density had originally been performed for a zero inlet swirl case. Since the inlet swirl is now at 62%, the previous mesh density sensitivities may have changed.

A general comparison was made between the tooth-on-rotor effective stiffness values of LabyXL and the tooth-on-stator values of CFX. Since the geometries for each seal were different, a direct comparison could not be made. However, it was shown that the effective stiffness values of the seals varied by 47.9 percent.

6.2 Eccentric Study

A study was performed to investigate the relationship between increasing eccentricity in a labyrinth seal and the forces produced. The forces were examined for eccentricity ratios from 0.1 to 0.6. There was little variation in the inlet pressures and inlet swirl in each case. The largest percent deviation in inlet pressure was 2.3%. The circumferential pressure and velocity distributions were shown to be fourth order polynomials. The dynamic coefficients were found for each eccentricity ratio and are shown in Table 6-2.

Table 6-2. CFX Dynamic Coefficients for Varying Eccentricity Ratios.

Eccentricity Ratio	Direct Stiffness (N/m)	Cross-coupled Stiffness (N/m)	Direct Damping (N-s/m)	Cross-Coupled Damping (N-s/m)	Effective Stiffness (N/m)
0.1	-3.821E+05	2.643E+06	1.015E+03	-8.457E-02	1.931E+06
0.2	-1.290E+06	2.207E+06	1.290E+03	-1.260E-01	2.207E+06
0.3	-1.459E+06	2.531E+06	1.198E+03	-1.422E-01	2.531E+06
0.4	-1.422E+06	2.658E+06	1.287E+03	-1.191E-01	2.658E+06
0.5	-1.131E+06	1.839E+06	9.577E+02	-1.303E-01	1.839E+06
0.6	-9.902E+05	1.902E+06	8.536E+02	-1.254E-01	1.902E+06

It was shown that the radial forces vary linearly with respect to eccentricity ratio. The tangential forces were shown to vary nonlinearly with respect to eccentricity ratio. It was suggested the nonlinearity may occur due to the fluctuation of inlet swirl in each case. This suggestion came about because it was shown that there is a relationship between the normalized tangential forces and the inverse of the normalized inlet swirl for each eccentricity.

6.3 Future Work and Recommendations

The major issue identified in this research is the need for a result independent mesh. The result independent mesh will require several things. The first item it requires is a license of ANSYS-CFX that allows for more nodes to be used in a solution. Next, it requires a new meshing scheme with mapped-mesh type qualities. Finally, the result independent mesh should also be independent of the inlet swirl value used in the labyrinth seal. If it is impossible for the result independent mesh to be independent of inlet swirl, then a result independent mesh should be created for each inlet swirl (or range of inlet swirls).

Additionally, if TASCflow is to be used for high inlet swirl values, a new mesh sensitivity study should be performed. Since the previous TASCflow mesh sensitivity study was performed at zero inlet swirl, it is possible that the mesh sensitivities have changed for the higher inlet swirl values now being used. Having result independent meshes for both CFX and TASCflow should resolve many of the issues presented in this paper.

References

- [1] Alford, J.S. (1965). Protecting turbomachinery from self-excited rotor whirl. *Journal of Engineering for Power*, v. 87, 333-344.
- [2] Benckert, H. Wachter, J. (1980). Flow induced spring coefficients of labyrinth seals for application in rotor dynamics. *NASA CP 2133*, 189-212.
- [3] Kirk, R.G. (1988). Evaluation of aerodynamic instability mechanisms for centrifugal compressors – part II: advanced analysis. *Journal of Vibration, Acoustics, Stress, and Reliability in Design*, v. 110, 207-212.
- [4] Rajakumar, C. Sisto, F. (1990). Experimental investigations of rotor whirl excitation forces induced by labyrinth seal flow. *Journal of Vibration, Acoustics, Stress, and Reliability in Design*, v 112, 263-272.
- [5] Wyssmann, H.R., Pham T.C., Jenny R.J. (1984). Prediction of stiffness and damping coefficients for centrifugal compressor labyrinth seals. *Journal of Engineering for Gas Turbines and Power*, v 106, 920-926.
- [6] Rhode D.L. Sobolik S.R. (1986). Simulation of subsonic flow through a generic labyrinth seal. *Journal of Engineering for Gas Turbines and Power*, v. 108, 674-680.
- [7] Rhode D.L., Hensel S.J., Guidry M.J. (1993). Three-dimensional computations of rotordynamic force distributions in a labyrinth seal. *Tribology Transactions*, v 36, 461-469.
- [8] Ishii E., Kato C., Katsuaki K., Ueyama Y. (1997). Prediction of rotordynamic forces in a labyrinth seal based on three-dimensional turbulent flow computation. *JSME International Journal Series C*, v. 40(4), 743-748.
- [9] Moore, J.J. (2003). Three-dimensional CFD rotordynamic analysis of gas labyrinth seals. *Journal of Vibration and Acoustics*, v 125, 427-433.
- [10] Kirk, R.G., Raju K.V.S., Ramseh, K. (1999). PC-based analysis of turbomachinery vibration. *The Shock and Vibration Digest*, v 31(6), 449-454.
- [11] Mehta, R.P. (2008). Labyrinth seal preprocessor and post-processor design and parametric study. Master of Science Thesis, Virginia Polytechnic Institute and State University.

- [12] Kocur, J.A., Nicholas, J.C., Lee, C.C. (2007). Surveying tilting pad journal bearing and gas labyrinth seal coefficients and their effect on rotor stability. *Proceedings of the Thirty-Sixth Turbomachinery Symposium*.
- [13] Kirk, R.G. Guo Z. (2004). Calibration of labyrinth seal bulk flow design analysis predictions to CFD simulation results. *IMECHE 8th International Conference on Vibrations in Rotating Machinery*.
- [14] Hirano, T., Guo, Z., Kirk R.G. (2005). Application of computational fluid dynamics analysis for rotating machinery – part II: labyrinth seal analysis. *Journal of Engineering for Gas Turbines and Power*, v 127, 1-7.
- [15] Kirk R.G. Guo Z. (2009). Influence of leak path friction on labyrinth seal inlet swirl. *Tribology Transactions*, v. 52, 139-145.
- [16] API Standards (Oct. 28, 2008). Retrieved Mar. 4, 2009, from <http://www.api.org/Standards>
- [17] Childs, D.W. (1993). *Turbomachinery rotordynamics: Phenomena, modeling, and analysis*. New York: Wiley.
- [18] ANSYS Workbench 11.SP 1 (2007). *Release 11 Documentation for ANSYS Workbench*.

Appendix A: Solution Run Times

Table A-1. Run Data for the Whirl Speed Study.

Whirl Percent	Whirl Speed (RPM)	Run Number	Number of Nodes	Run Time (hr:min:sec)	Iterations
100	21662	1	37741	0:20:33	149
		2	93109	0:07:30	16
		3	128051	0:10:14	15
		4	176943	0:10:27	12
		Total		0:48:44	192
86.33	18700	1	37741	0:19:57	146
		2	93109	0:08:01	19
		3	128051	0:29:21	51
		4	176943	0:12:40	13
		Total		1:09:59	229
75	16246.5	1	37741	0:17:07	144
		2	93109	0:08:04	22
		3	128051	0:30:04	60
		4	176943	0:13:01	16
		Total		1:08:16	242
60	13000	1	37741	0:19:59	169
		2	93109	0:10:16	29
		3	128051	0:34:11	68
		4	176943	0:18:58	24
		Total		1:23:24	290
50	10831	1	37741	0:22:07	188
		2	93109	0:14:15	40
		3	128051	1:15:59	155
		4	176943	0:27:45	35
		Total		2:20:06	418
30	6500	1	176943	2:29:46	268
		2	176943	4:04:08	307
		Total		6:33:54	575
25	5415.5	1	37741	0:21:24	199
		2	93109	1:35:28	293
		3	128051	1:10:53	150
		4	176943	2:02:59	162
		Total		5:10:44	804

15	3250	1	176943	2:34:54	268
		2	176943	4:10:07	321
		Total		6:45:01	589
		Average		3:10:01	417

Table A-2. Run Data for the Eccentricity Study.

Eccentricity Ratio	Eccentricity (in)	Whirl Speed (RPM)	Run Type	Number of Nodes	Run Time (hr:min:sec)	Iterations
0.1	0.0005	21662	Laminar	201531	0:44:12	61
			Turbulent	201531	5:28:35	349
			Total		6:12:47	410
0.1	0.0005	16246.5	Laminar	201531	0:43:23	61
			Turbulent	201531	5:53:58	374
			Total		6:37:21	435
0.2	0.001	21662	Laminar	201768	0:44:20	62
			Turbulent	201768	5:14:25	332
			Total		5:58:45	394
0.2	0.001	16246.5	Laminar	201768	0:17:58	22
			Turbulent	201768	5:56:25	373
			Total		6:14:23	395
0.3	0.0015	21662	Laminar	201309	0:49:21	63
			Turbulent	201309	5:18:15	338
			Total		6:07:36	401
0.3	0.0015	16246.5	Laminar	201309	0:48:09	63
			Turbulent	201309	5:34:25	354
			Total		6:22:34	417
0.4	0.002	21662	Laminar	201042	0:50:22	64
			Turbulent	201042	5:35:06	341
			Total		6:25:28	405
0.4	0.002	16246.5	Laminar	201042	0:52:43	64
			Turbulent	201042	6:00:15	353
			Total		6:52:58	417
0.5	0.0025	21662	Laminar	212059	0:50:51	63
			Turbulent	212059	5:57:51	349
			Total		6:48:42	412
0.5	0.0025	16246.5	Laminar	212059	0:55:16	63
			Turbulent	212059	6:32:59	369
			Total		7:28:15	432

0.6	0.003	21662	Laminar	217311	0:59:40	65
			Turbulent	217311	6:26:48	339
			Total		7:26:28	404
0.6	0.003	16246.5	Laminar	217311	1:01:07	65
			Turbulent	217311	6:31:19	359
			Total		7:32:26	424
			Average		6:40:39	412

Appendix B: Whirl Speed Variation Study Flow Characteristics

ANSYS

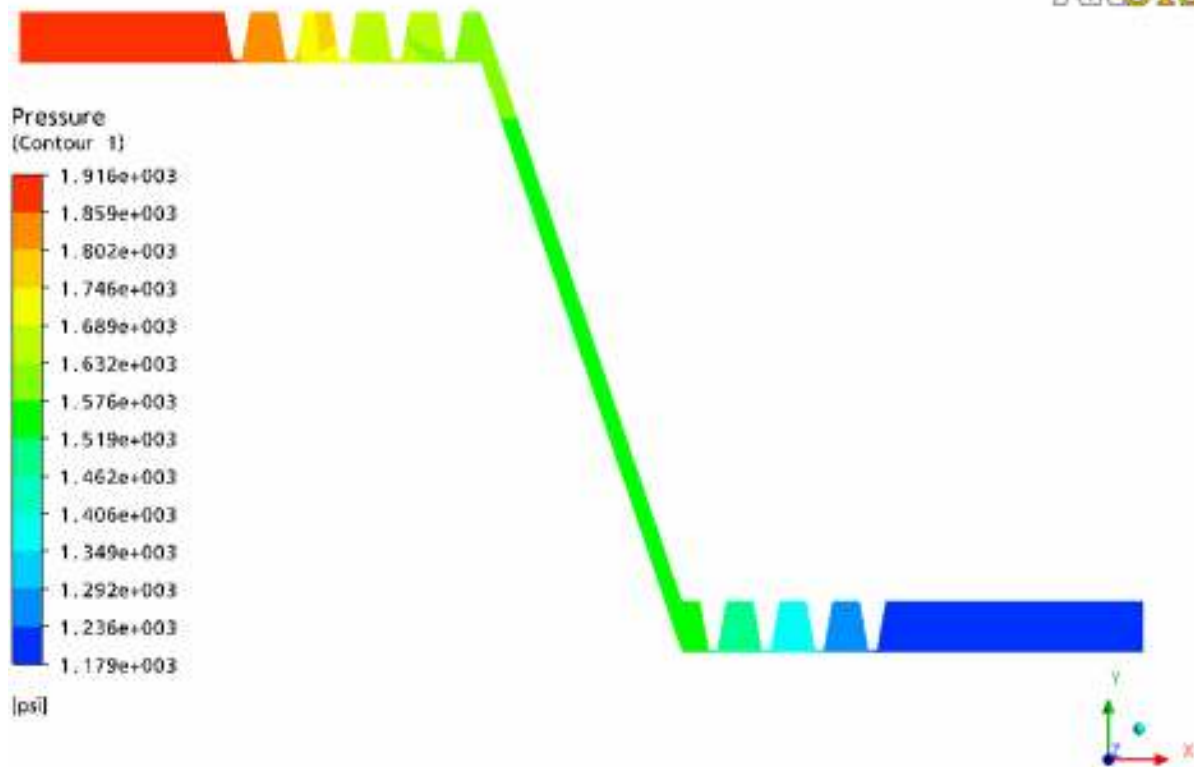


Figure B-1. Pressure Contour of the Entire Seal.

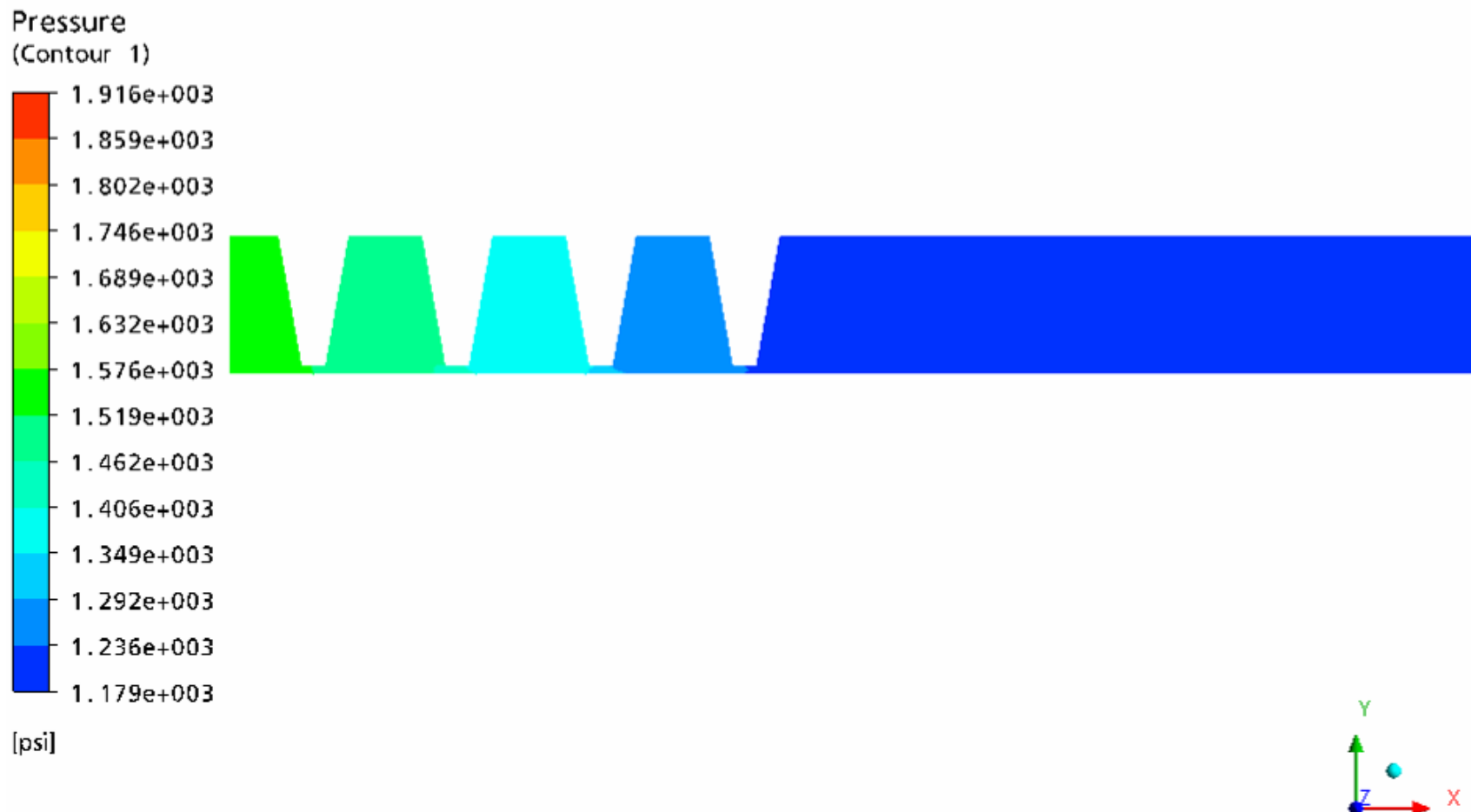


Figure B-2. Pressure Contour of API Seal.

Velocity in Stn Frame
(Contour 1)

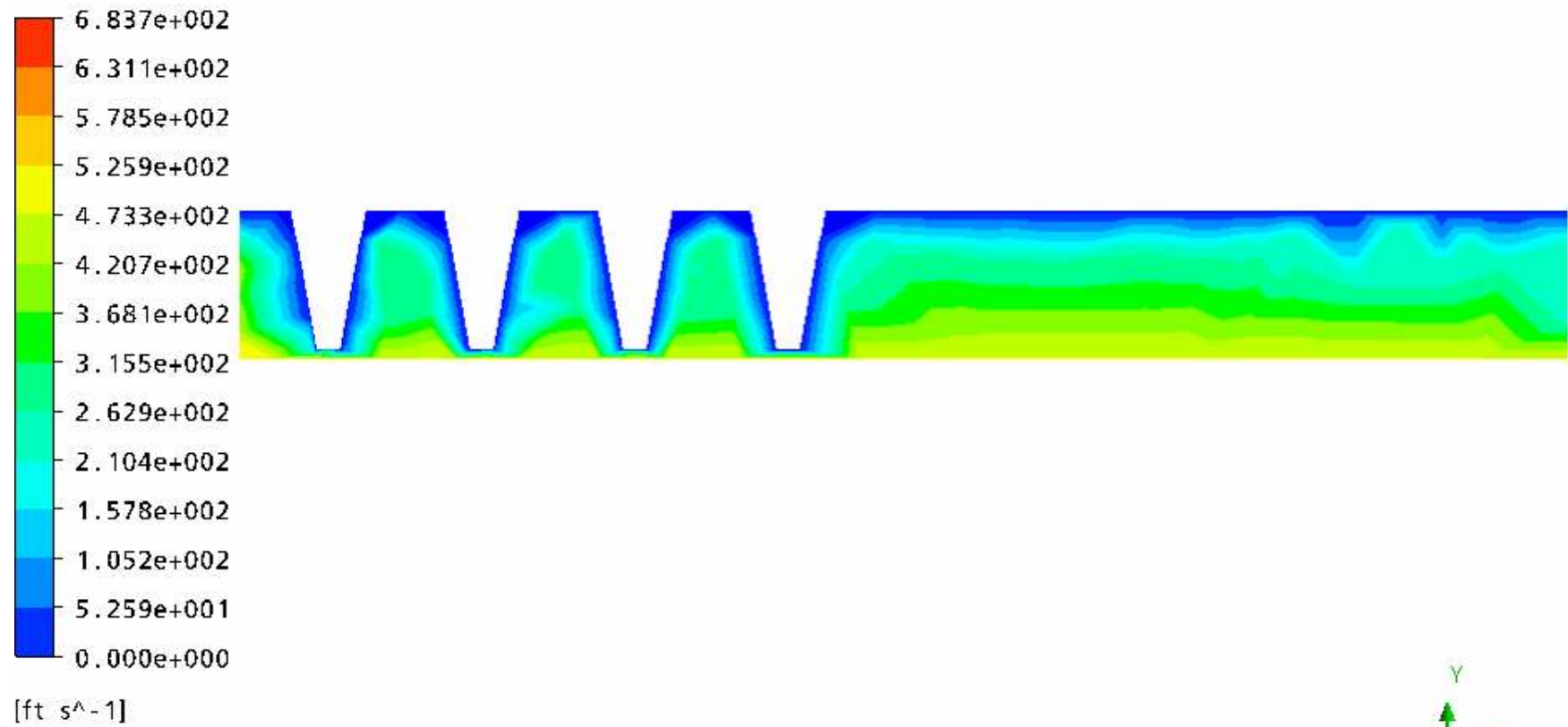


Figure B-3. Stationary Frame Velocity Contours.

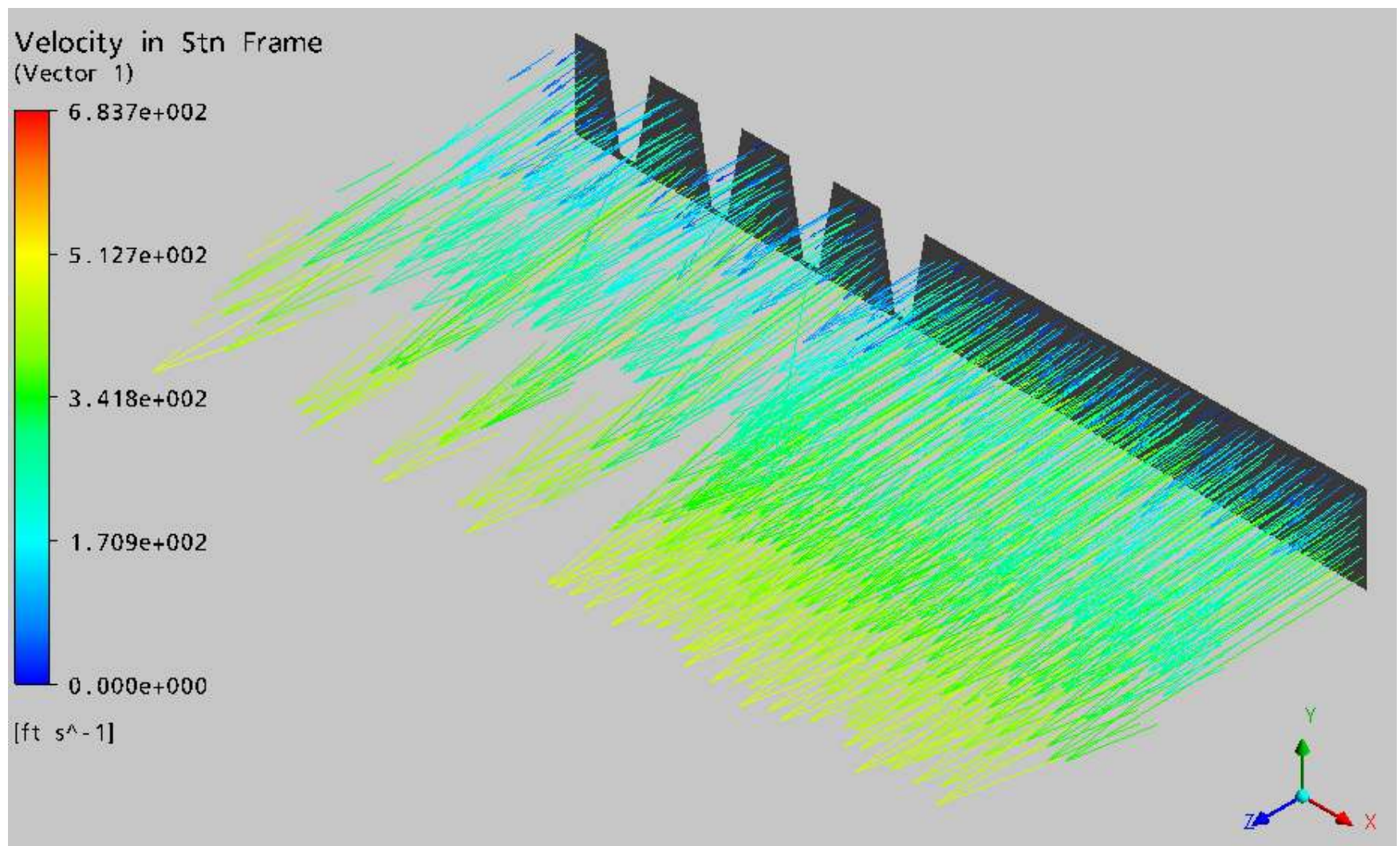


Figure B-4. Stationary Frame Velocity Vectors.

Velocity in Stn Frame
(Streamline 1)

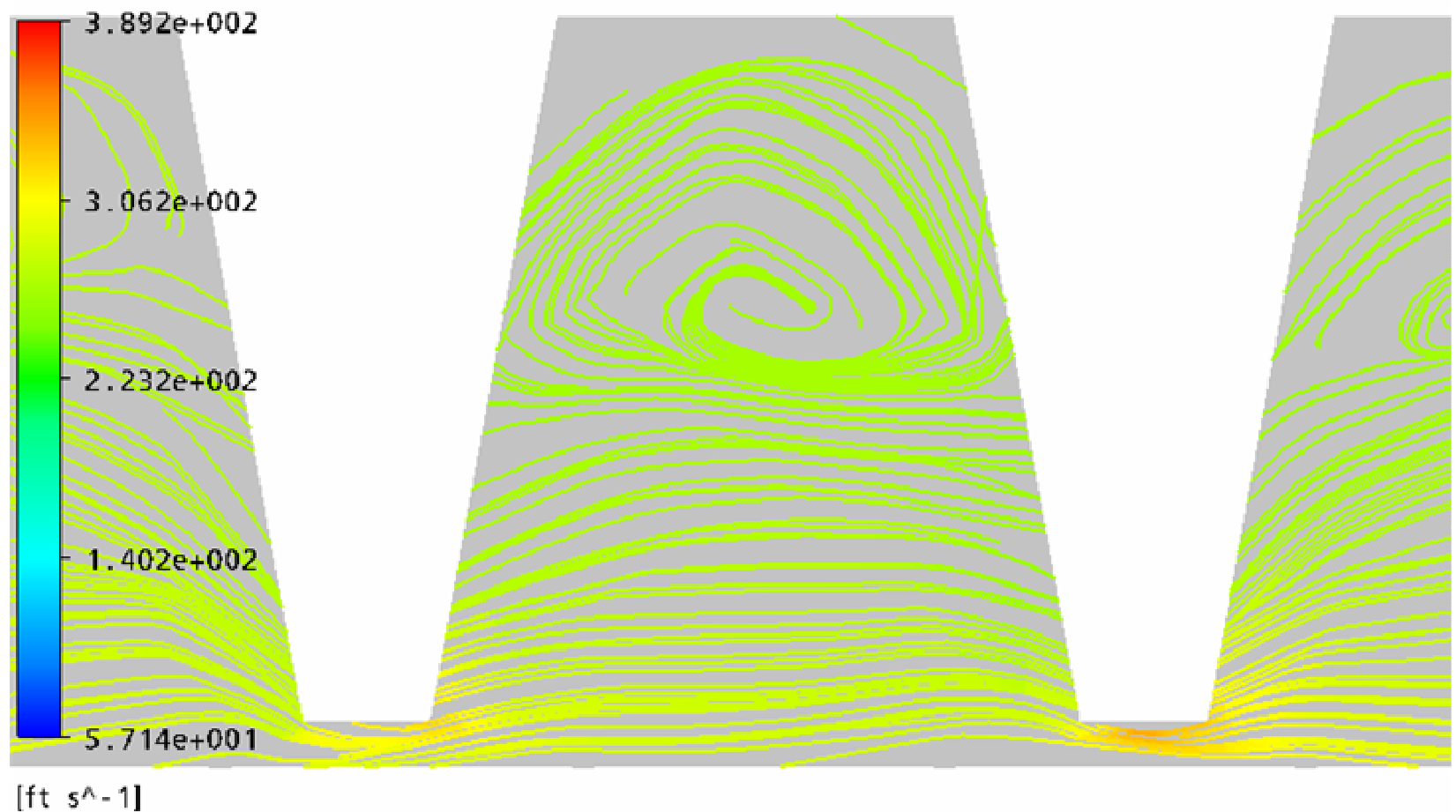


Figure B-5. Stationary Frame Velocity Streamlines Between Second and Third Teeth.

Appendix C: Eccentricity Variation Study Flow Characteristics

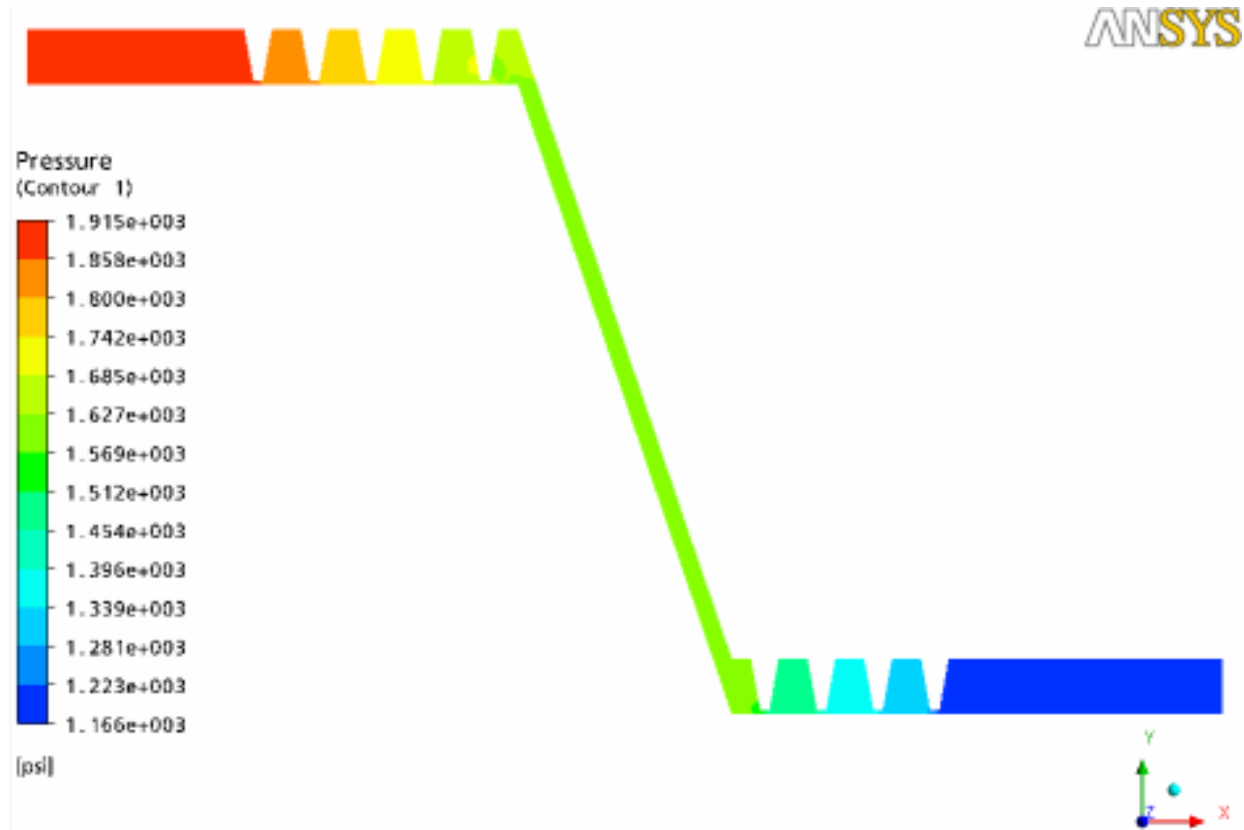


Figure C-1. Full Seal Pressure Distribution.

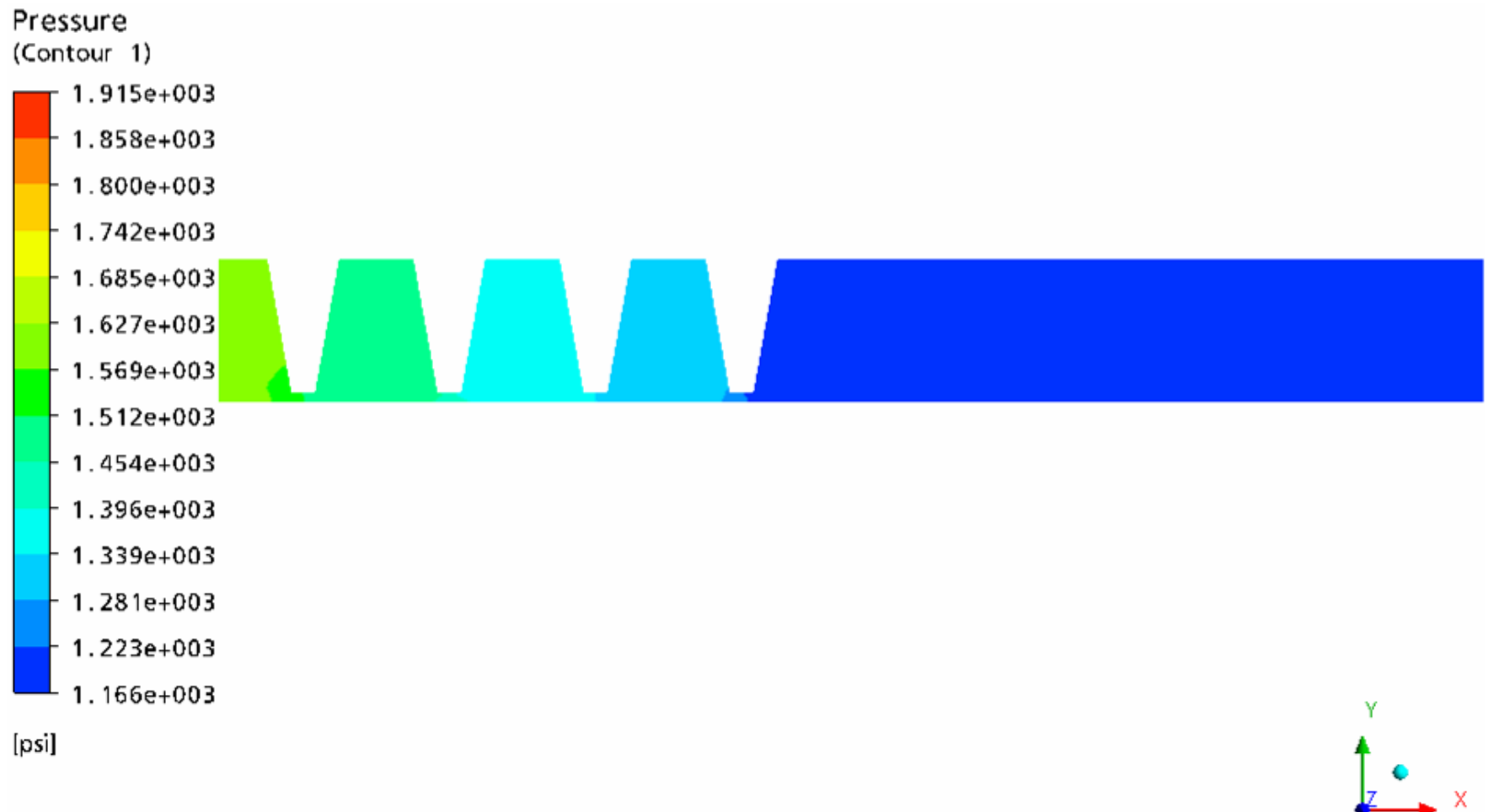
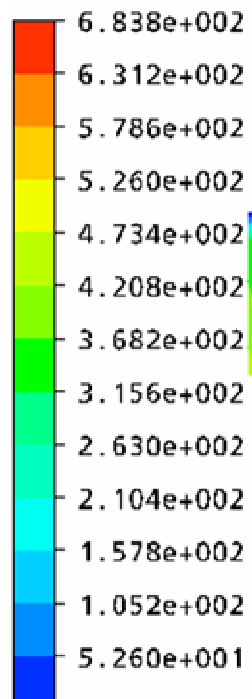


Figure C-2. API Seal Pressure Distribution.

Velocity in 5tn Frame
(Contour 1)



[ft s⁻¹]

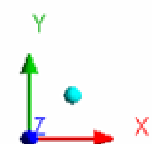
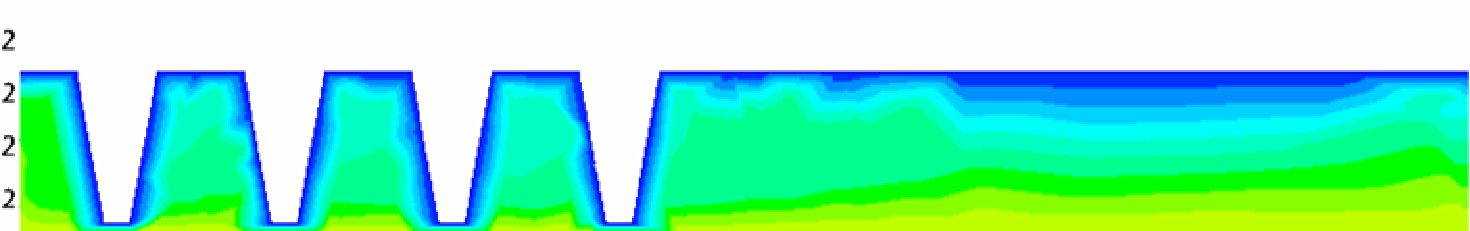


Figure C-3. Stationary Frame Velocity Contours.

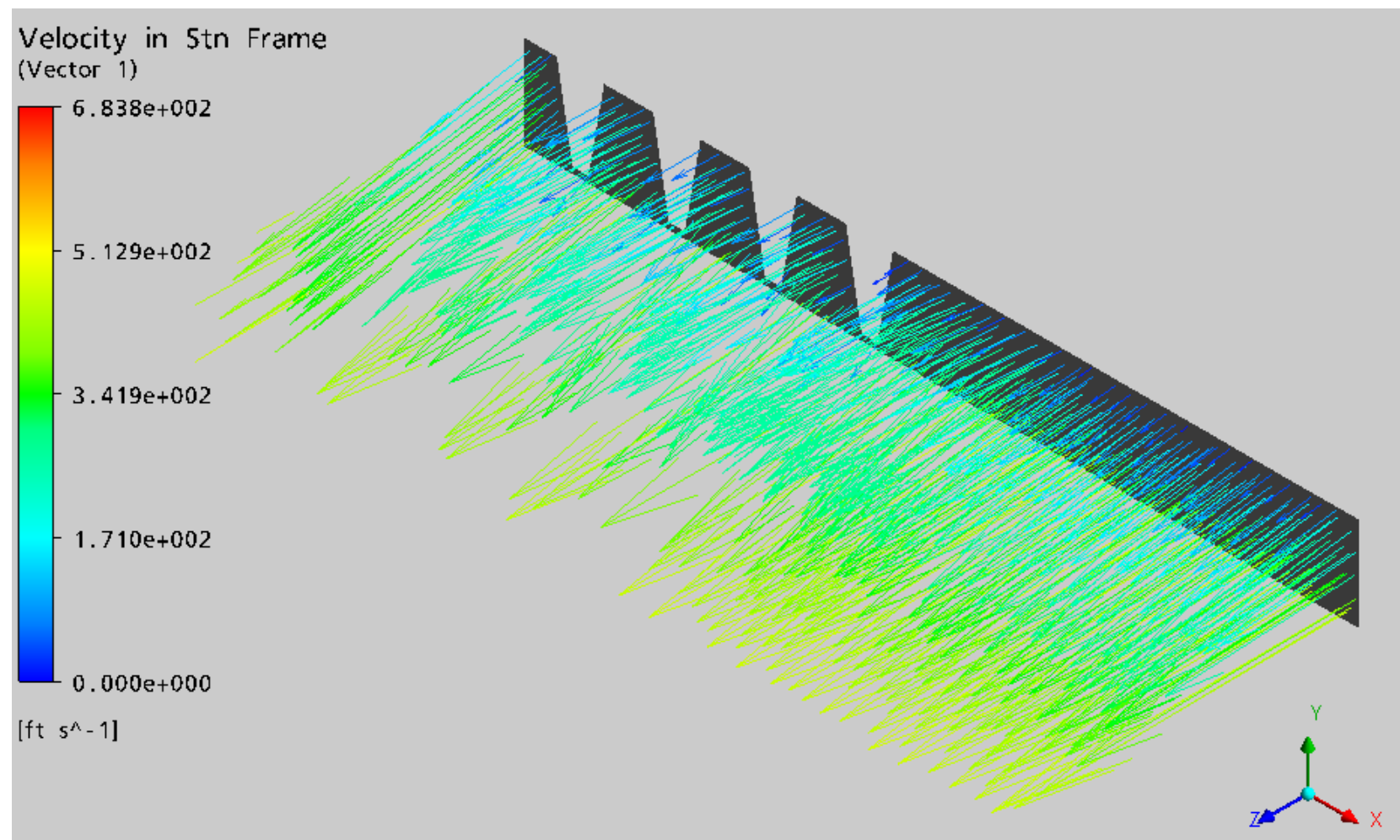
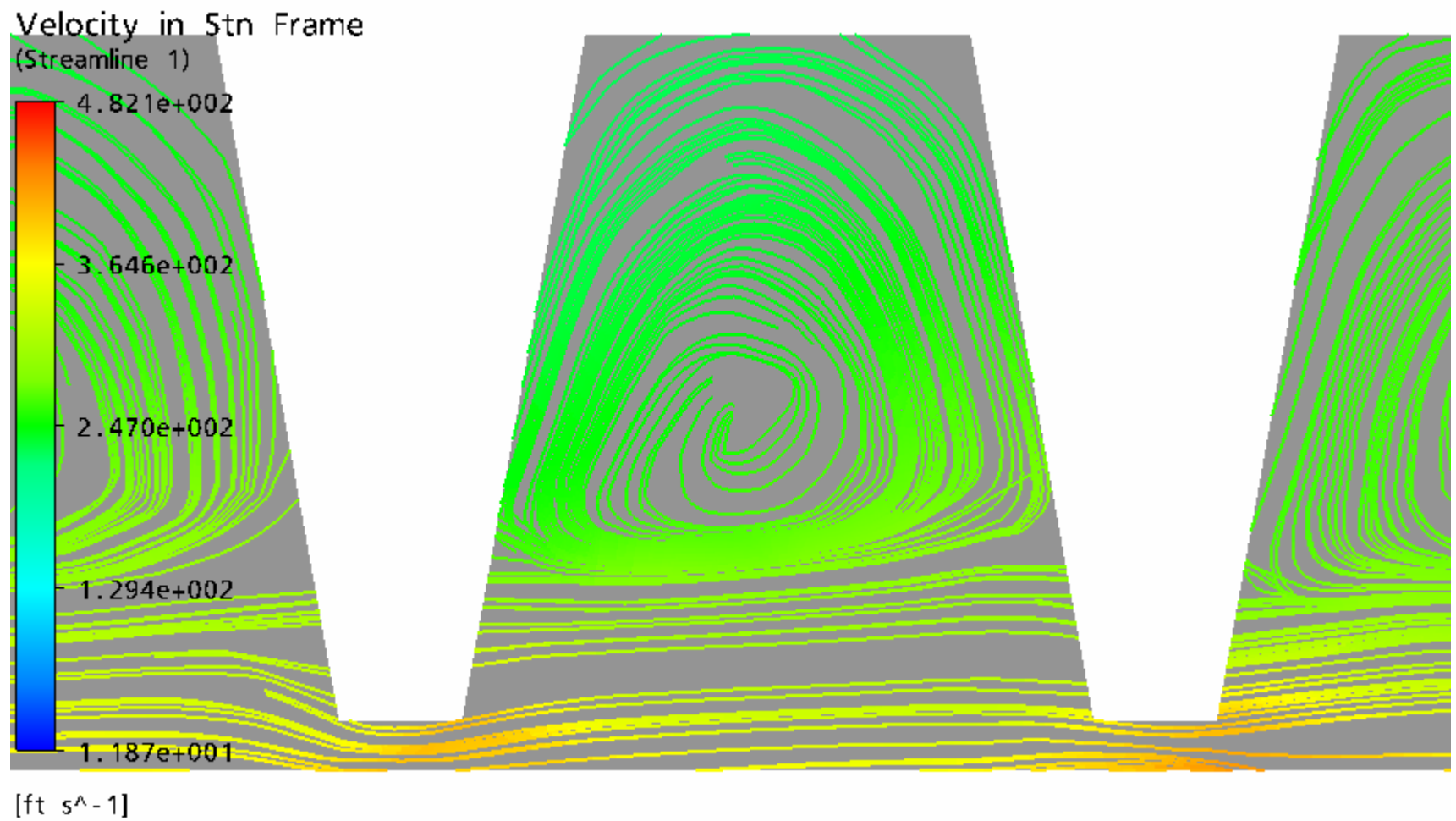


Figure C-4. Stationary Frame Velocity Vectors.



C-5. Stationary Frame Velocity Streamlines Between Third and Fourth Teeth.